Corrosion Science 246 (2025) 112759

Contents lists available at ScienceDirect

Corrosion Science

journal homepage: www.elsevier.com/locate/corsci

On the impact of Cr and Ag additions on the grain boundary microchemistry, hydrogen permeability and environmentally assisted cracking mechanism of an Al-Zn-Mg-Cu-Zr 7xxx alloy

Chijioke Kenneth Akuata [a], Oliver Beyß [a], Lisa.T. Belkacemi [b,c], Kerstin Hantzsche [b], Matthew E. Curd [d], Daniela Zander [a,e,*]

[a] Chair of Corrosion and Corrosion Protection, Foundry Institute, Division of Materials Science and Engineering, RWTH Aachen University, Intzestraße 5, Aachen 52072, Germany
[b] Leibniz-Institute for Materials Engineering – IWT, Badgasteiner Straße 3, Bremen 28359, Germany
[c] MAPEX Center for Materials and Processes, University of Bremen, Bibliothekstraße 1, Bremen 28359, Germany
[d] Department of Materials, Henry Royce Institute, University of Manchester, M13 9PL, UK
[e] Deutsches Zentrum für Luft, und Raumfahrt (DLR), German Aerospace Center, Institute of Materials Physics in Space, Linder Höhe, Cologne 51147, Germany

ARTICLE INFO

Keywords:
7xxx aluminum alloys
Grain boundary microchemistry
Hydrogen permeation
Hydrogen trapping
Hydrogen environmentally assisted cracking (HEAC)
Hydrogen embrittlement

ABSTRACT

This study explored the impact of minor Cr and Ag additions on the resistance of a new generation Al-8Zn-2Mg-2Cu-0.1Zr alloy to hydrogen environmentally assisted cracking (HEAC) in humid air. The results show that HEAC in Al-8Zn-2Mg-2Cu-0.1Zr alloy can be suppressed by 0.1 wt% Cr addition, due to the formation of E-$Al_{18}Mg_3Cr_2$ dispersoids with a high H binding energy and possibly a less electrochemically active grain boundary (GB) microchemistry. ~ 0.3 wt% Ag addition in Al-8Zn-2Mg-2Cu-0.1Zr alloy had no influence on the HEAC susceptibility, despite 1 at% Ag partitioning in the GB η-$Mg(Zn,Cu,Al)_2$ and a minor decrease in the PFZ width.

1. Introduction

The new generation Al-Zn-Mg-Cu (7xxx) aluminum alloys were developed in the last three decades owing to the growing demand for weight reductions, energy efficiency, improved mechanical properties and cost optimization in the aerospace industry [1,2]. The enhanced properties in these alloys, such as superior strength, fracture toughness and through-thickness properties were achieved by increasing the Zn/Mg ratio, lowering the Cu and impurity (Fe and Si) levels and replacing Cr and Mn with Zr for recrystallization inhibition [2–4]. However, such alloy chemistry modifications have a significant influence on the final grain structure, as well as the size and chemistry of the grain boundary η-$Mg(Zn,Cu,Al)_2$ precipitates (GBPs), all of which can influence an alloys susceptibility to environmentally assisted cracking (EAC) [5–8].

EAC in aqueous environments or in humid air results in the brittle fracture of a susceptible ductile material, especially when loaded in the short transverse (ST) orientation [5,9–11]. The generally accepted mechanisms of EAC in aqueous environment (also known as stress corrosion cracking, SCC) are preferential anodic dissolution of the GBPs and hydrogen embrittlement [12,13]. Furthermore, SCC, e.g. in 0.6 M NaCl solution, is characterized by extensive corrosion such as pitting or intergranular corrosion (IGC) that results in the formation of critical defects which transition into cracks under suitable loading and testing conditions [14,15]. On the contrary, during EAC in humid air, crack initiation and propagation are solely due to hydrogen H embrittlement with no strong evidence of macroscopic corrosion [8]; hence hydrogen environmentally assisted cracking (HEAC) is often used to describe this phenomenon. Moreover, oxidation of Al or the partial dissolution of the anodic GBPs or the coarse Mg_2Si particles can occur in humid air, thereby facilitating H_2O reduction and H generation at high fugacity, followed by subsequent diffusion, trapping and embrittlement of the material [16].

HEAC initiation on a smooth 7xxx alloy surface takes place preferentially at sites characterized by high local stress concentrations and micro-crack formation during mechanical deformation (hot rolling) [7,

* Corresponding author at: Chair of Corrosion and Corrosion Protection, Foundry Institute, Division of Materials Science and Engineering, RWTH Aachen University, Intzestraße 5, Aachen 52072, Germany.
E-mail address: d.zander@gi.rwth-aachen.de (D. Zander).

https://doi.org/10.1016/j.corsci.2025.112759
Received 28 October 2024; Received in revised form 19 January 2025; Accepted 30 January 2025
Available online 31 January 2025

9]. These include the interface of coarse intermetallic particles (IMPs) such as Mg_2Si, Al_7Cu_2Fe and S-Al_2CuMg [5,17,18] or at surface-linked pores [19]. The crack initiation stage is comprised of a sequence of localized events that includes the transition from the initial condition after exposure to the test conditions to the precursor stage, followed by the incubation period and finally the formation of proto-cracks and their concomitant transition to short and long cracks [20–22]. Crack growth proceeds discontinuously as often indicated by striations, known as crack arrest marks (CAMs) [22,23]. This periodic crack growth behavior during HEAC results from the slow or limited supply of H atoms ahead of the crack tip to sustain the growth process that occurs when the threshold H concentration is reached [11,16,24,25]. Therefore, H entry, transport and trapping in the alloy are crucial in the understanding of the HEAC mechanism.

The H embrittlement mechanism in 7xxx alloys can be explained by models such as Hydrogen Enhanced Decohesion (HEDE) [26,27], Hydrogen Enhanced Localized Plasticity (HELP) [28] and Adsorption Induced Dislocation Emission (AIDE) [29,30]. The fracture mode is mainly intergranular (IG) and occurring at high angle grain boundary (HAGB) [5,8,9,16]. Therefore, alloy chemistry, which affects the grain structure, recrystallized fraction and the GB microstructure and microchemistry (GBP size, GBP composition, segregation and the precipitate free zone (PFZ) width), play a significant role in an alloy's susceptibility. Transgranular (TG) quasi-cleavage fracture has also been observed after tensile deformation in hydrogen charged high-strength 7xxx alloys [31–33] and after alternate immersion in 0.6 M NaCl solution [13].

New generation 7xxx alloys (e.g. 7449, 7085) are more sensitive to HEAC relative to the conventional alloys (e.g. 7075 and 7050) and this is related to the alloy chemistry [5,7]. The high Zn/Mg ratio (≥ 4) of the new generation alloys exceeds the recommended limit of 2 – 3 for optimum environmentally-induced cracking resistance [34]. This, in addition to the lower Cu content, results in a GB microchemistry that is detrimental to HEAC performance relative to the conventional alloys [6]. Furthermore, the significant reduction in the recrystallized volume fraction in the third-generation alloys results in a favorable grain structure for sustained crack propagation [5,7,35].

An in-depth understanding of HEAC and the quest for mitigation approaches in high-strength 7xxx alloys are key in driving future alloy development for optimum performance. In Cu-containing alloys, heat treatment 'regimen' such as rapid quenching and overaging (T7x) can produce a GB microstructure that is more resistant to HEAC compared to the peak aged (T6) condition [9,16]. Although not directly proven, decreasing the PFZ width is also proposed to be beneficial in suppressing H embrittlement, since the PFZ is vulnerable to local deformation [36]. A more recent approach is the H partitioning concept, which involves H trapping in the interior of IMPs or precipitates with high H binding energy, thereby limiting H diffusion and trapping at GBs and at the interface of coarse IMPs and precipitates [32,33,36–38]. This can suppress HEAC by delaying the time to reach the critical H concentration necessary to induce decohesion at interfaces [16].

This study aimed to explore two alloy chemistry modifications, namely Cr and Ag additions that could potentially suppress HEAC in 7449 alloy. Cr forms E-$Al_{18}Mg_3Cr_2$ dispersoids for recrystallization inhibition and reduction in the fraction of HAGBs which is beneficial for environmentally-induced cracking resistance [39–41]. Furthermore, the high trapping energy of the E-$Al_{18}Mg_3Cr_2$ phase, deduced from density functional theory (DFT) calculations [32], indicates a potential HEAC suppression by H trapping in its interior that remains to be explored. Ag, on the other hand, enhances matrix precipitation and suppresses PFZ formation in low-medium Zn 7xxx alloys [42], which has been proposed to be beneficial in HEAC suppression. Also, it was hypothesized that the formation of a Ag-rich GB η-$Mg(Zn,Cu,Al)_2$ with Ag addition could reduce its reactivity in humid air, thus suppressing the local H production rate and improving HEAC resistance. The assessment of the influence of Cr and Ag on the GB microstructure/microchemistry and H permeation enabled an understanding of their impact on the HEAC mechanisms of a new generation 7xxx alloy.

2. Material and methods

2.1. Alloy composition and processing

The investigated Al-8Zn-2Mg-2Cu-0.1Zr base alloy has a Zn:Mg ratio of ~ 4.0 and composition within the range of AA7449. Minor additions of 0.1 wt% Cr and 0.3 wt% Ag to the base (7449) alloy, were made to achieve the Cr-modified 7449 +Cr alloy and the Ag-modified 7449 +Ag alloy, respectively. The compositions of the investigated alloys determined by optical emission spectrometry (OES) on a Hitachi High Tech 0E750 device are shown in Table 1.

The alloys were cast as plate of ~ 140 mm thickness, homogenized at 420 °C/5 h + 475 °C/24 h, followed by hot forging (strain rate = 0.1 s^{-1}) and hot rolling (strain rate ≈ 1.5 s^{-1}) in multiple passes at 400 – 460 °C to a final thickness of ~ 70 mm. The formed plates were solution treated at 475 °C for 2 h, water quenched and stabilized at room temperature (RT) for at least 3 days to achieve the T4 condition. Samples in T4 state were artificially aged in two steps; 121 °C/6 h + 163 °C/15 h followed by air-cooling to achieve the T76 state. A summary of the processing route of the alloys has been reported in a previous work [40].

2.2. Bulk and grain boundary microstructure characterization

Samples for Optical Light Microscopy (OLM), Scanning Electron Microscopy (SEM) and Electron Backscatter Diffraction (EBSD) were cold embedded, ground successively using silicon carbide (SiC) paper and then polished using diamond suspension and SiO_2-based oxide polishing suspension. Coarse intermetallic particles (IMPs) characterization and EBSD measurements were done using a Zeiss Supra 55 VP (Carl Zeiss Microscopy, Germany), equipped with an energy-dispersive X-ray spectroscopy (EDX) detector and an EBSD detector from Oxford Instruments, UK. Characterization of the primary IMPs phase fraction (PF) was performed on SEM backscattered electron (BSE) images using the image threshold function in Image J [43]. The SEM images used were taken at lower magnification to show a better distribution of the primary phases and to accurately characterize the phase fraction. EBSD measurements for grain size and recrystallized volume fraction characterization were performed on the longitudinal-short transverse (L-ST) plane with a step-size of ~ 3.8 μm. To characterize the dislocation density after processing, measurements were done in refined accuracy mode using a step size of ~ 1.0 μm. Analysis of the acquired EBSD maps was done using AztecCrystal software from Oxford Instruments, UK.

Characterization of the GB η-$Mg(Zn,Cu,Al)_2$ size and chemistry were performed on samples prepared by Xe^+ plasma focused ion beam (PFIB) using a Thermo Scientific Helios 5 Hydra UX DualBeam PFIB-SEM. The HAGB for the PFIB lift-outs were identified by EBSD mapping of a marked region of interest (ROI) on polished sample surfaces. After the lift-outs, the lamellae for Scanning Transmission Electron Microscopy (STEM) EDX analysis were attached to a Mo grid, thinned in multiple steps until electron transparent and finally cleaned at a low voltage of 5 kV to eliminate any beam damage from the thinning steps. Precipitates characterization, particularly the GB η-$Mg(Zn,Cu,Al)_2$ phase was done by STEM using a JEOL JEM-F200 device operated at a 200 kV acceleration voltage and equipped with an Oxford Instruments EDX detector and a GATAN OneView high-resolution (HR) camera. To support the STEM-EDX results of the GB η-$Mg(Zn,Cu,Al)_2$ chemistry and equally precisely measure the segregation levels at the GBs, Atom Probe Tomography (APT) analysis was performed using a Cameca LEAP 5000XR device. The APT sample preparation, measurements and 3D reconstruction of the investigated volume were carried out according to the procedure described in a previous work [44].

Table 1
Composition of alloys in wt%.

Composition (wt%)	Al	Zn	Mg	Cu	Zr	Ti	Fe	Si	Cr	Ag
7449	Bal.	7.63	1.97	1.72	0.10	0.027	0.08	0.06	-	-
7449 +Cr	Bal.	7.62	1.97	1.64	0.10	0.027	0.08	0.10	0.10	
7449 +Ag	Bal.	7.63	1.82	1.66	0.10	0.027	0.08	0.12	-	0.33

2.3. Hydrogen permeation

Hydrogen permeation tests to investigate the trapping capacity of the alloys were performed in a Devanathan-Stachurski electrochemical double cell. The set-up consists of a thin sample membrane (prepared from the alloys) secured between two independent cells as depicted in Fig. 1. The membranes were prepared to ensure H diffusivity is in the short transverse (ST) direction, with thickness ranging ~ 50 – 100 μm. On one side of the foil, the native oxide was removed by plasma etching since it can act as a H diffusion barrier [45,46], followed by physical vapor deposition (PVD) of ~ 50 nm layer of Palladium (Pd) to act as a tracer for diffusing H.

The thin-membrane served as the working electrode (WE), while a saturated calomel electrode (SCE) was used as the reference electrode (RE). Prior to H charging, cleaning of the Pd surface was done according to the procedures established in previous investigations [47–49]. H charging was performed under open circuit corrosion in 0.01 M NaOH solution (pH ~ 12) and at RT, where H atoms generated at high fugacity on the sample surface diffuses through the material due to concentration gradient. The detection of the diffusing H was done under open circuit potential (OCP) in 0.1 M phosphate buffer solution (PBS) with a pH of ~ 7 and at RT. H detection at OCP on the exit cell is defined by the potential decay transient and stabilization at about – 0.7 V_{SCE} due to the transformation of the Pd layer to PdH_x by H saturation [48,49]. Using the Time-lag approach in Eq. 1 [50], the permeation time was analogously defined as the time at which 63 % ($t_{0.63}$) of the Pd potential transient has decayed before reaching steady state at – 0.7 V_{SCE}.

$$t_{0.63} = \quad L^2/6D_H \tag{1}$$

$t_{0.63}$ = permeation time (s), L = sample membrane thickness (cm) and D_H = effective H diffusion coefficient ($cm^2\ s^{-1}$).

Since H charging was done under open circuit corrosion, the membrane thickness for calculating the D_H according to Eq. (1) was defined as the average of the initial and final thickness. The final membrane thickness after permeation was determined by mass loss measurements after immersion in 0.01 M NaOH for different durations corresponding to the permeation measurements. Samples with area ranging from 4.5 – 6 cm^2 were used for the immersion test. After immersion, the samples were cleaned with running water, and then with ethanol and dried. This was followed by etching in concentrated HNO_3 for 1 minute to remove the corrosion products, as outlined in the ASTM G1 standard [51]. The corrosion rates were calculated from mass loss according to Eq. (2)

$$Corrosion\ rate(\mu m/h) = (\Delta m \times 10^4)/(A \quad \times t \quad \times \rho) \tag{2}$$

Δm = mass loss (g), A = sample area (cm^2), t = immersion time (h) and ρ = density, 2.85 (g cm^{-3})

2.4. Constant load (CL) HEAC test

The smooth-round tensile specimens for the mechanical test as well as the CL-HEAC test were machined in the through-thickness (ST) orientation, according to the geometry shown in Fig. 2. Immediately after machining, the samples were cleaned in deionized water, followed by 5 minutes cleaning in an ultrasonic bath with ethanol to remove any cutting fluid residue, and then dried.

Mechanical tests were performed on a Zwick Roell Kappa 100 DS device at a strain rate of $2.5 \times 10^{-4}\ s^{-1}$ in order to determine the yield strength (0.2 % proof stress: $\sigma_{0.2}$) of the alloys. The CL-HEAC samples were spring-loaded at 50 % of the determined $\sigma_{0.2}$ at 70 °C and 85 % relative humidity (RH) using a loading frame described in a previous work [5]. The loaded samples were exposed in the climate chamber and the temperature was ramped up and held at 70 °C for ~ 2 h to ensure uniform temperature within the chamber and on the sample surfaces, thus hindering water condensation on the samples when the RH is being ramped up to 85 % for the test. The HEAC susceptibility was defined by the time-to-failure (HEAC-Lifetime) in the climate chamber under the test conditions (70 °C and 85 % RH). After failure, the samples were removed from the climate chamber and stored in a desiccator. 'Post--mortem' analysis of the fracture surfaces and the gauge section were done by SEM-EDX imaging in secondary electron (SE) and backscatter electron (BSE) mode.

3. Results

3.1. Microstructure and grain boundary micro-chemistry characterization

On the bulk microstructure characterization, Fig. 3(a) – (c) show the SEM-BSE images of the coarse primary IMPs, namely Al_7Cu_2Fe and Mg_2Si, determined by EDX. No significant difference in the primary phase fraction (PF) was observed. A phase fraction (PF) of 9(± 0.3) %, 9 (± 1.7) % and 11(± 2.0) % were estimated in 7449, 7449 +Cr and 7449 +Ag, respectively. The EBSD results of the grain size (GS), recrystallized fraction (Rex) and stored energy by geometrically

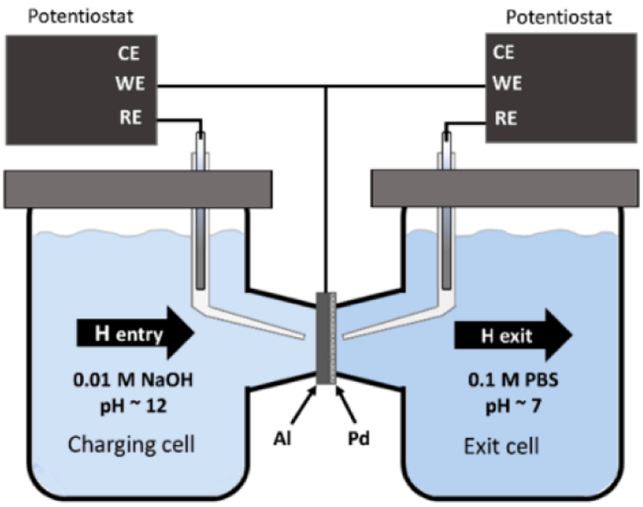

Fig. 1. Schematic illustration of the Devanathan-Stachurski electrochemical double-cell set-up used for H permeation measurements.

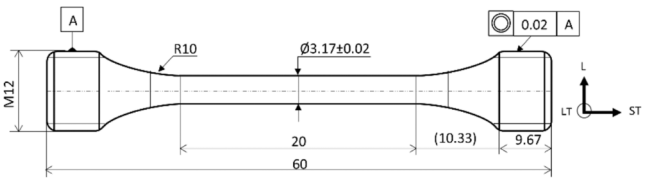

Fig. 2. Geometry of smooth-round tensile specimen for mechanical and HEAC tests.

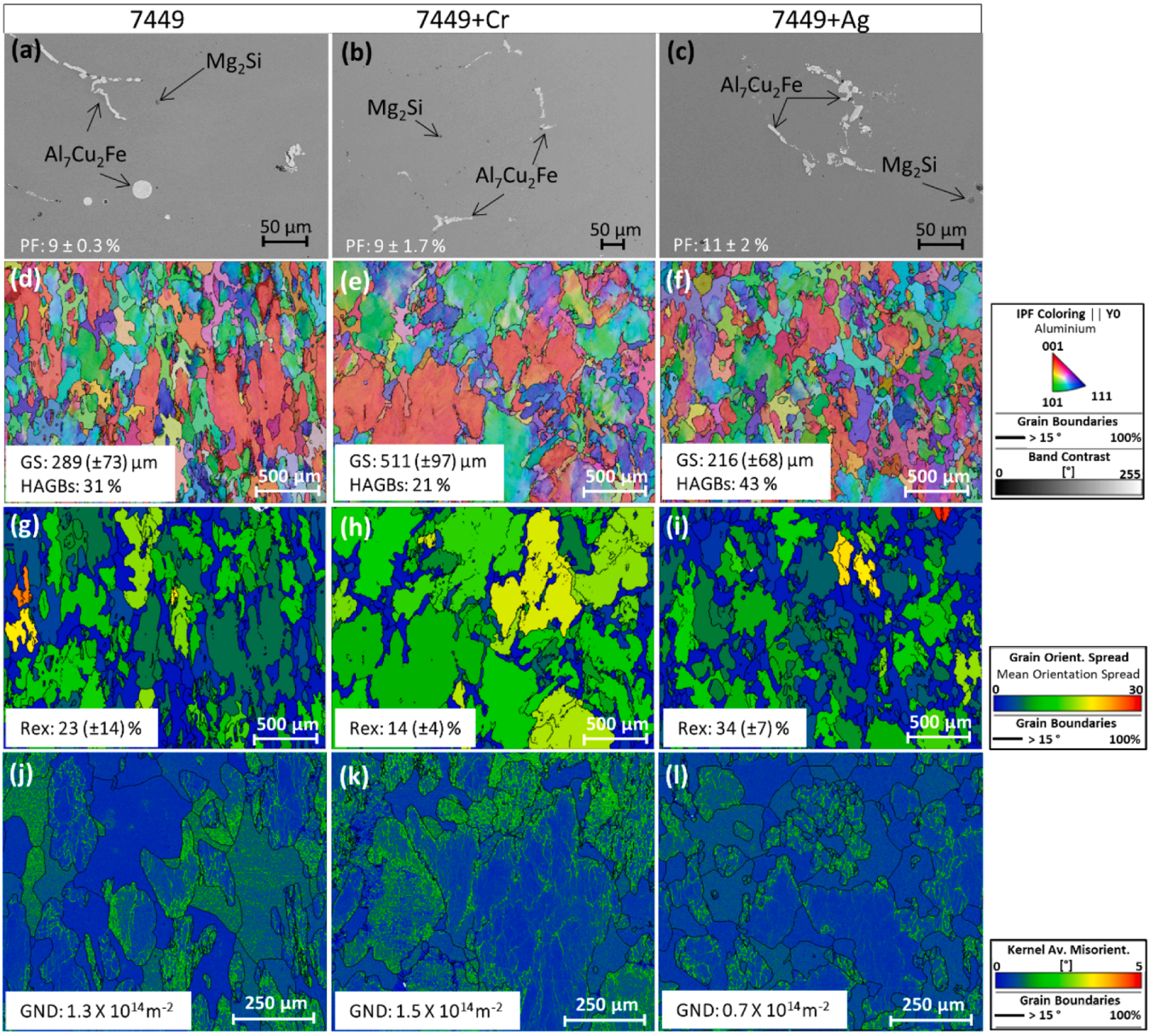

Fig. 3. SEM and EBSD characterization of bulk T76 microstructure of 7449, 7449 +Cr and 7449 +Ag: (a) – (c) SEM-BSE images showing coarse IMPs, (d) – (f) IPF maps showing average grain size and fraction of HAGBs, (g) – (i) GOS maps showing Rex fraction and (j) – (l) KAM maps showing GND density in alloys. All values presented indicates the average ± the standard deviation.

necessary dislocation density (GND) are shown in Fig. 3(d) – (l). The inverse pole figure (IPF) maps in Fig. 3(d) – (f) show an average grain size of 289 (± 73) µm, 511 (± 97) µm and 216 (± 68) µm in 7449, 7449 +Cr and 7449 +Ag, respectively. The fraction of HAGB (%) showed an opposite trend, with 7449 +Cr having a lower amount of 21 % while 7449 +Ag had a higher fraction of 43 %, with respect to the base alloy with 31 % HAGBs. The grain orientation spread (GOS) maps showing the Rex fraction (%) are presented in Fig. 3(g) – (i). With Cr addition, a decrease in the Rex fraction from 23 (± 14) % in 7449 to 14 (± 4) % in 7449 +Cr was observed. On the contrary, Ag addition increased the Rex fraction to 34 (± 7) %. These are consistent with the aforementioned HAGBs fraction observed in the modified alloys relative to the base alloy, as well as the GND density shown by the kernel average misorientation (KAM) maps in Fig. 3(j) – (l), where a GND density of 1.3×10^{14} m^{-2}, 1.5×10^{14} m^{-2} and 0.9×10^{14} m^{-2} were measured in 7449, 7449 +Cr and 7449 +Ag, respectively. A decrease in the Rex fraction with Cr addition in 7449 has been reported in a previous work [40] and is related to the presence of the E-$Al_{18}Mg_3Cr_2$ dispersoids, which increased the overall dispersoid volume fraction for Rex inhibition and increased the Zener pinning force. The higher Rex fraction in 7449 +Ag could be related to the decreases in the stacking fault energy (SFE) with Ag addition [52].

On the grain boundary precipitate characterization, Fig. 4(a) – (c) show the PFIB SEM images, with red boxes showing the investigated HAGBs. The corresponding dark-field (DF) STEM images in Fig. 4(d) – (f) show the GBP (η Mg(Zn,Cu,Al)$_2$ phase) on the HAGBs and the adjacent PFZ. The E-$Al_{18}Mg_3Cr_2$ dispersoids were occasionally identified at the GBs in 7449 +Cr, with large η Mg(Zn,Cu,Al)$_2$ phase heterogeneously formed at its interface. The results of the GBP size from 24, 30 and 33 η Mg(Zn,Cu,Al)$_2$ precipitates in 7449, 7449 +Cr and 7449 +Ag, respectively, and the PFZ width are shown in Table 2.

From the results of the GBP (η Mg(Zn,Cu,Al)$_2$ phase) length and width in Table 2, it is clear that Cr and Ag additions in 7449 did not significantly alter the average GBP size. Although heterogeneous

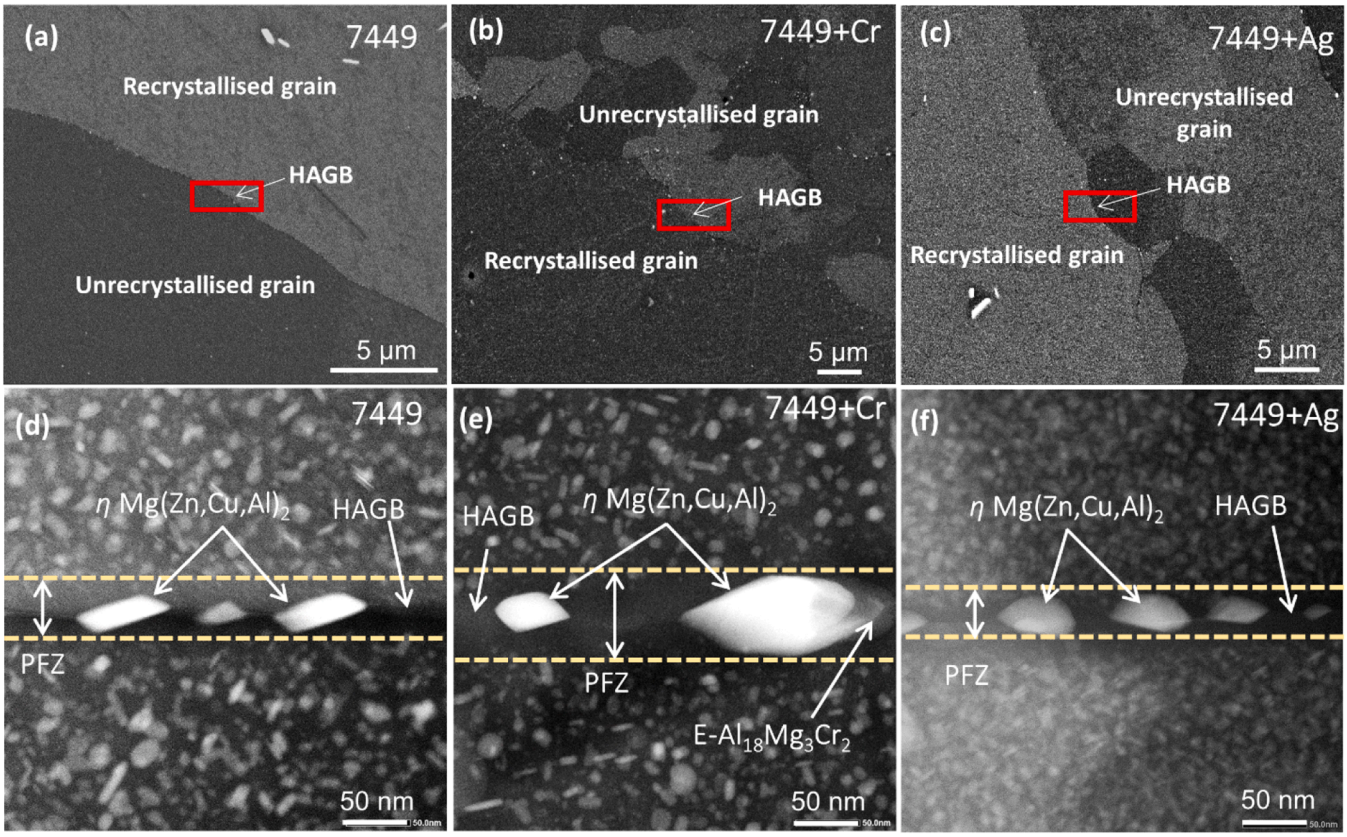

Fig. 4. (a) – (c) PFIB-SEM showing region of HAGBs lift-out for STEM investigation of grain boundary precipitation after T76 aging. (d) – (f) show the corresponding DF-STEM images showing a typical GB microstructure in 7449, 7449 +Cr and 7449 +Ag, respectively. For interpretation of the references to color in this figure legend, the reader is referred to the web version of this article.

Table 2
Summary of the effect of Cr and Ag on GBP size, spacing and PFZ width in 7449.

Alloy	GBP length (nm)	GBP width (nm)	GBP spacing (nm)	PFZ width (nm)
7449-T76	80 ± 58	26 ± 11	50 ± 24	45 ± 3
7449 +Cr-T76	73 ± 30	30 ± 11	94 ± 66	55 ± 9
7449 +Ag-T76	75 ± 43	21 ± 6	47 ± 26	39 ± 2

nucleation of coarse η $Mg(Zn,Cu,Al)_2$ phase at the E/Al interface at the GB was observed in 7449 +Cr, this did result in a higher average GBP size. Nonetheless, this resulted in a larger inter-particle (GBP) spacing and the PFZ width in 7449 +Cr relative to the base alloy. On the other hand, Ag addition did not show a significant influence on the GBP spacing, but had only a marginal influence on the PFZ width, which decreased from 45 ± 3 in the 7449 alloy to only 39 ± 2 after Ag addition. These demonstrate a decrease in the GB coverage by precipitates in 7449 +Cr, as shown by the much larger GBP spacing. Based on these results, it can be concluded that the GB coverage by precipitates increased as follows: 7449 = 7449 +Ag > 7449 +Cr.

The chemistry of the GB η phase determined by Cliff-Lorimer (CL) extrapolation [6,44] of the STEM-EDX results are shown in Table 3. This involved 14 EDX point measurements for 7449 and 7449 +Ag and 8 measurements for 7449 +Cr as shown in Figure A.1 in the Appendix. CL extrapolation was done by fixing the generally known average Mg content of the η phase at 33 at% [6,53,54]. From Table 3, a decrease in the Al content and an increase in the Zn and Cu content of the GBP phase in 7449 +Cr compared with the base alloy can be seen. A similar trend in the Al and Zn content of the GBP was also observed in the Ag modified alloy. However, the Cu content of the GBP in this case remained similar to that of the base alloy and only ~ 1 at% Ag was determined, which is close to the amount reported in a previous investigation after T76 aging [44].

Table 3
GB η $Mg(Zn,Cu,Al)_2$ composition by CL extrapolation of STEM-EDX point analysis.

	Composition (at%)				
Alloy	Mg	Zn	Cu	Al	Ag
7449-T76	33	40	9	18	-
7449 +Cr-T76	33	46	15	6	-
7449 +Ag-T76	33	44	8	14	1

The high Cu content and low Al content of the GB η phase in 7449 +Cr could be attributed to the quench sensitivity effect of Cr. As can be seen in Fig. 4(e), large (possibly quench induced) η phase are formed at the E/Al interface at the GB. η phase formed during quenching in 7xxx plates are large and differ in composition with their counterparts formed during aging [6].

The APT results of the grain boundary (GB) microchemistry are depicted in Fig. 5. The 3D reconstruction images and 1D composition profiles of the GB η precipitate and solute segregation in 7449, 7449 +Cr and 7449 +Ag are shown in Fig. 5(a) – (c), (d) – (f) and (g) – (i), respectively. The average composition results of the GB η phase show that the Mg content ranges between ~ 32 – 35 at% in these alloys. Furthermore, the Al content of this phase was found to be higher (~ 7.7 at%) in 7449 +Cr relative to the measured amount in 7449 (~ 4.8 at %). Nonetheless, a comparable amount of Zn (53 – 54 at%) and Cu (5.3 – 5.6 at%) were determined in the GB η phase in both alloys.

In 7449 +Ag, the GB η phase had an Al content of ~ 12.9 at%, which far exceeds the amount determined in 7449. Contrary to the observation with the 7449 and 7449 +Cr, a slightly lower Zn and Cu content of ~

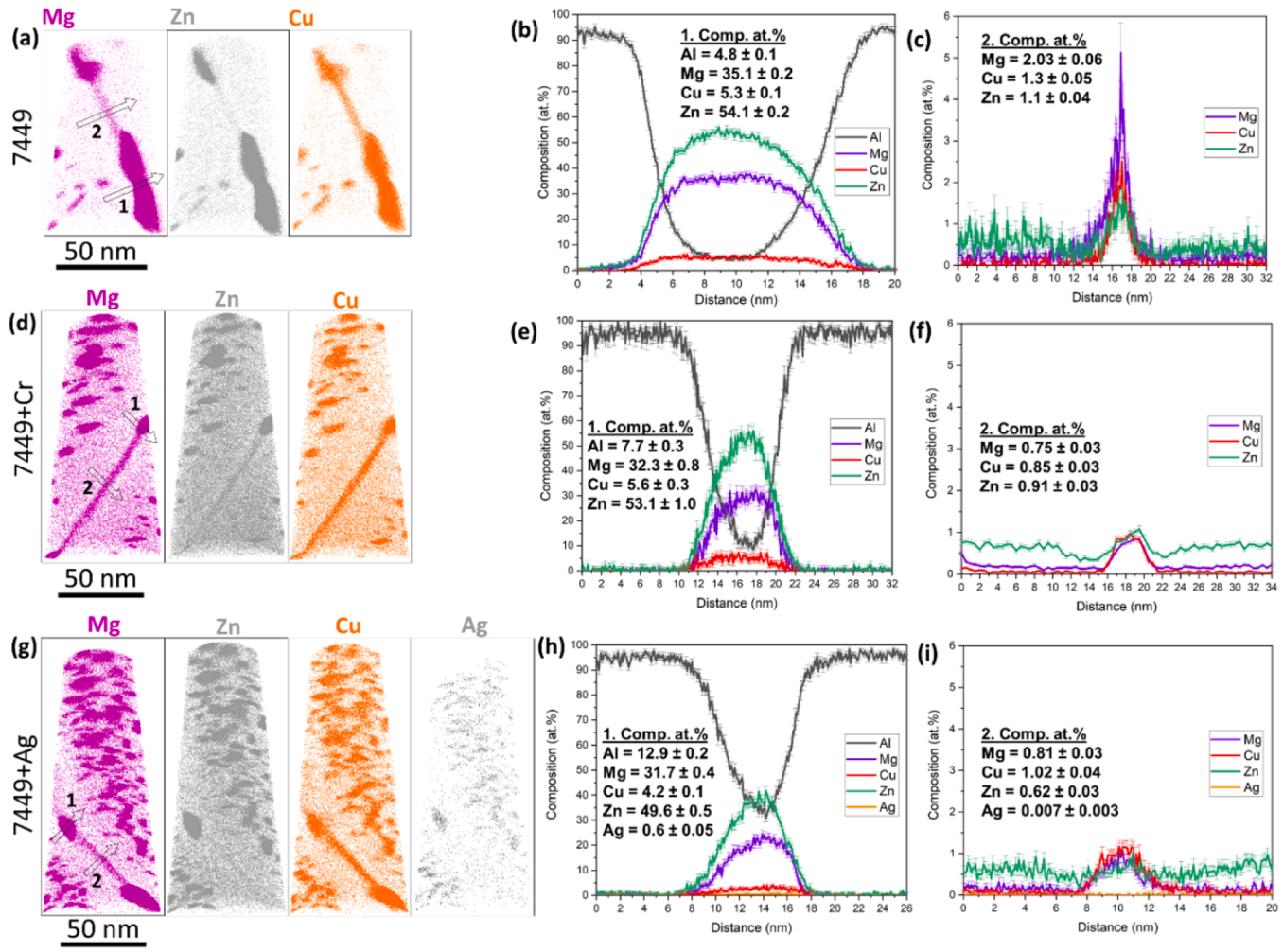

Fig. 5. APT 3D reconstruction images and the corresponding 1D composition profile of the GB η $Mg(Zn,Cu,Al)_2$ phase and segregation: (a) – (c) 7449 (d) – (f) 7449 +Cr (g) – (i) 7449 +Ag. Regions marked 1 and 2 in (a),(d),(g) represent measured positions for the 1D composition profiles, while the inserts in the profiles are the average compositions (GB η and segregation). For interpretation of the references to color in this figure legend, the reader is referred to the web version of this article.

49.6 at% and 4.2 at%, respectively, were determined. Ag partitioning of up to ~ 0.6 at% was determined with this technique, which is close to the 1 at% determined by STEM-EDX (CL extrapolation). The GB η phases observed by APT, particularly in 7449 +Cr, are assumed to be aging-induced because of their differences in composition (Cu content) which is discussed further in the discussion section. Minor solute incorporation at the GBs was observed, with the average segregation levels of Mg, Zn and Cu in 7449 +Cr and 7449 +Ag being low ($\leq$ 1 at%). But, a slightly higher average Mg segregation (~ 2 at%) was observed in the 7449. No GB segregation of Ag was observed in 7449 +Ag, which agrees with an earlier work [44].

Fig. 6(a) – (e) shows the TEM images of the plate-shaped E-$Al_{18}Mg_3Cr_2$ dispersoid formed on a HAGB and extending into the adjacent grain interiors in 7449 +Cr, with heterogeneous nucleation of η Mg $(Zn,Cu,Al)_2$ phase at the interface of E-plate edges at the HAGB.

The formation of E dispersoids and the quench-induced η phase in the matrix, on the GBs (or across it) depletes solute atoms and vacancies that are crucial for precipitation during artificial aging. This is believed to be responsible for the decreased grain boundary (GB) coverage (higher η $Mg(Zn,Cu,Al)_2$ spacing) and decreased segregation level of Mg observed in 7449 +Cr alloy by APT relative to 7449 alloy. The HRTEM and the corresponding Fast Fourier Transform (FFT) images of an E dispersoid and a large η phase are shown in Fig. 6(f) and (g), respectively. The inverse FFT (IFFT) images of the interfaces of E/Al (purple box) and η/Al (green box) in Fig. 6(h) and (i), respectively, show series of misfit dislocations which is an evidence of lattice misfit at the E and η phase interfaces with the Al matrix. E dispersoids are known to be incoherent with the Al-matrix, which explains the high quench sensitivity of Cr-containing 7xxx alloys [4,39,55,56]. Furthermore, coarse η precipitates are equally incoherent with the Al matrix [57]. These observations are relevant for hydrogen trapping in the 7449 +Cr alloy.

3.2. Hydrogen permeability under free corrosion

The results of the hydrogen permeation measurement are shown in Fig. 7. During H charging in 0.01 M NaOH as shown in the representative plots in Fig. 7(a), the Al side OCP increased rapidly to about — 1.4 V_{SCE} within the first few hours, owing to surface corrosion and subsequent H generation at high fugacity by H_2O reduction and by AlH_3 oxidation at the hydroxide/metal interface, according to Eqs. (3) – (6) [47,49]. No significant change in the Al OCP was observed for the remaining duration of the test, where a maximum potential of about — 1.35 V_{SCE} was measured. Additionally, only negligible differences in the Al OCP were observed with Cr and Ag addition, suggesting a comparable surface reaction kinetic and H activity.

$$Al + 4OH^- \rightarrow Al(OH)_4^- + 3e^- \quad (3)$$

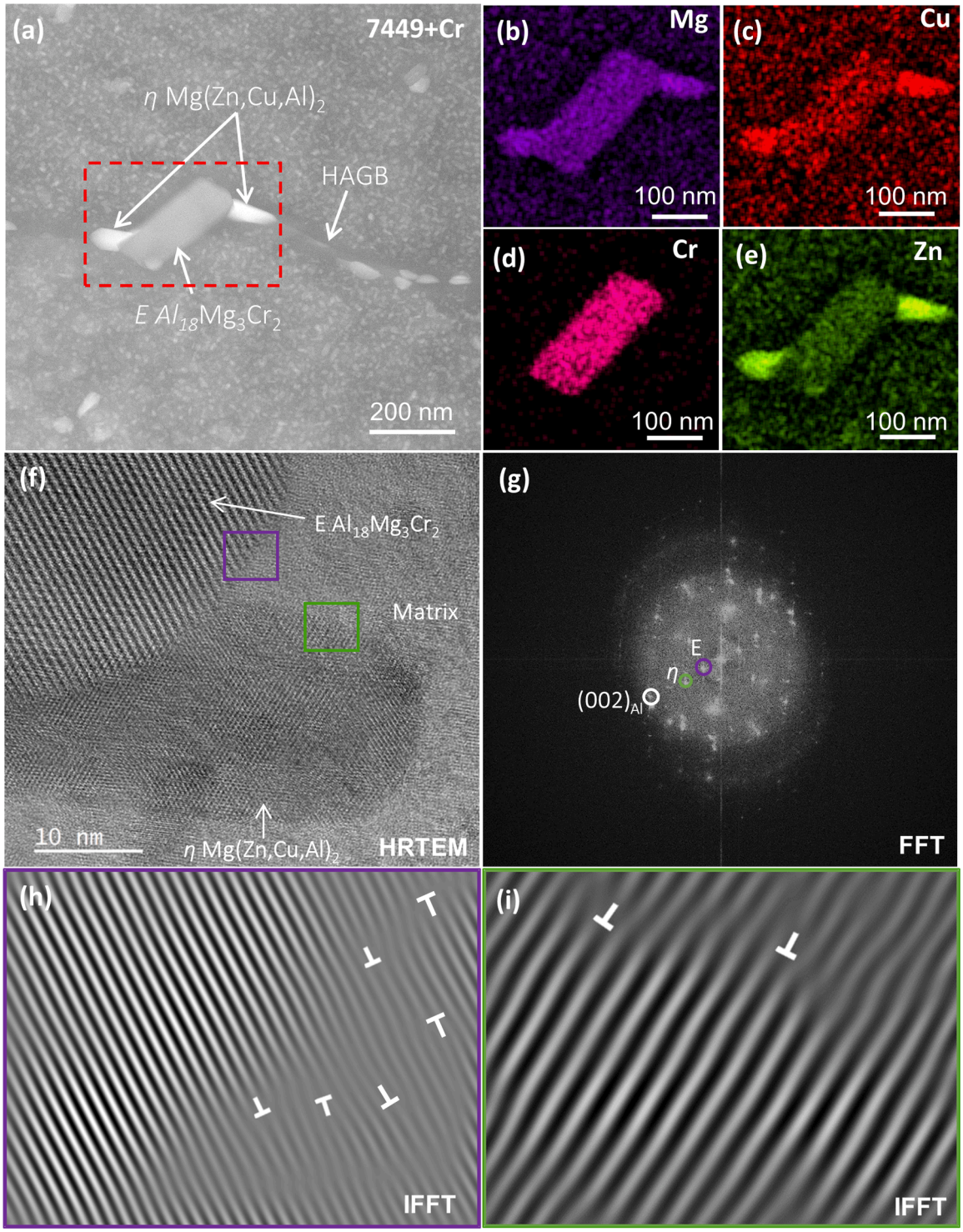

Fig. 6. DF-STEM image of E-dispersoid across a HAGB with heterogeneous formation of η at the interface (a) and the corresponding EDX maps (b) – (e) of the region shown by the red dashed box. HRTEM image of E/η/Al interface (f) and the corresponding FFT pattern (g). The IFFT of the E/Al and η/Al interface showing misfit dislocation are shown in (h) and (i), respectively. For interpretation of the references to color in this figure legend, the reader is referred to the web version of this article.

$$3H_2O + 3e^- \leftrightarrow 3H_{ads} + 3OH^- \quad (4)$$

$$Al + 3H_{ads} \rightarrow AlH_3 \quad (5)$$

$$AlH_3 + 3OH^- \leftrightarrow Al(OH)_3 + 3H_{ads} + 3e^- \quad (6)$$

Fig. 7(b) – (d) represent the measured Pd OCP in 0.1 M phosphate buffer solution (PBS) for 7449, 7449 +Cr and 7449 +Ag, respectively, and in different membrane thicknesses. In all three alloys, the Pd open circuit potential (OCP) remained constant at about 0.2 – 0.28 V_{SCE} for a duration which is directly proportional to the square of the membrane thickness, followed by a potential decay transient before reaching steady-state at ~ – 0.7 V_{SCE}, indicating H permeation from the Al side through the foil owing to concentration gradient and the concomitant transformation of the Pd layer to PdH_x [48,49]. A comparison of the

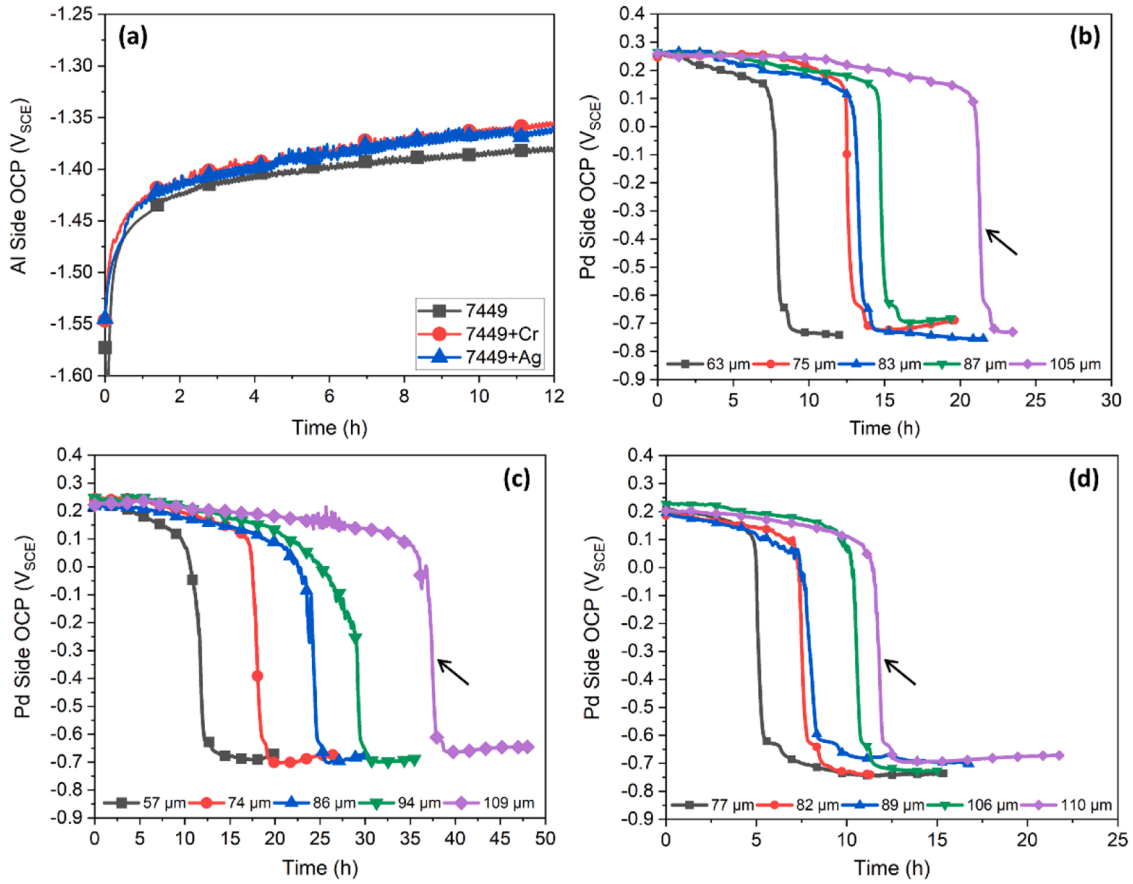

Fig. 7. (a) Al side OCP during H charging in 0.01 M NaOH (b) – (d) Pd side OCP in 0.1 M phosphate buffer solution for 7449, 7449 +Cr and 7449 +Ag, respectively and in different sample membrane thicknesses.

permeation time ($t_{0.63}$) in Fig. 7(b) – (d) which corresponds to a Pd OCP of about – 0.4 V_{SCE} show an increase in the permeation time with increasing sample membrane thickness. Furthermore, in membranes of a comparable thickness, e.g. 105 – 110 µm (arrow in plots), the permeation time increased as follows: 7449 +Ag < 7449 < 7449 +Cr.

3.3. Corrosion rate during permeation and Effective hydrogen diffusion coefficient (D_H)

Fig. 8 shows the results of the corrosion rate from Eq. (2) for determining the final membrane thickness after permeation test and calculating the D_H from Eq. (1). The SEM-BSE images in Fig. 8(a) – (c) for 7449, 7449 +Cr and 7449 +Ag, respectively, show the cross-section of the samples after 24 h of immersion in the 0.01 M NaOH. Irrespective of the slight deviations at coarse intermetallic particles (IMPs), the observed corrosion process was found to be mainly uniform on the entire cross-section and in all three alloys. However, the plots of the corrosion rate calculated at different immersion times and fitted with a power law function in Fig. 8(d) show that the corrosion rate is not constant, but rather varies with the immersion duration. A higher corrosion rate of 1.0 – 1.5 µm/h was observed at shorter immersion times, which then decreased rapidly (due to the build-up of corrosion products at the sample surface) and remained constant at ~ 0.1 µm/h after about 24 h of immersion. This observation agrees with the potential measurement during H charging (Fig. 7(a)), were the Al side OCP increases rapidly from — 1.55 to — 1.40 V_{SCE} within the first few hours and then remained relatively stable over time.

The thickness reduction (TR) after each permeation duration was estimated by integrating the area under the corrosion rate versus immersion time plot in Fig. 8(d) according to Eq. (7) and with respect to the power law equation of the fitted results for each alloy.

$$TR(\mu m) = \int_{t}^{t_{0.63}} CR\ dt \tag{7}$$

CR = Corrosion rate (µm/h) and dt = immersion duration/time until hydrogen permeation ($t_{0.63}$).

With the determination of the thickness reduction after permeation, the membrane thickness (L) in Eq. (1) was determined by averaging the initial and final thickness. Re-arranging Eq. (1) to the equation of a straight line and plotting $L^2/6$ against $t_{0.63}$ as shown in Fig. 8(e), the permeation results were fitted with a linear function with slope = D_H and 0 intercept, which strongly obeys Fick's law of diffusion. On this basis, D_H reflects H diffusivity in the presence of metallurgical traps, potential vacancy-H injection due to NaOH corrosion and the possible influence of surface oxides/hydroxides [47,49]. According to Fig. 8(e), a D_H of 2.2×10^{-10} cm^2/s, 1.3×10^{-10} cm^2/s and 4.5×10^{-10} cm^2/s were determined for 7449, 7449 +Cr and 7449 +Ag, respectively. The individually determined D_H for different foil thicknesses used for the plot in Fig. 8(e) are shown in Table A.1 (Appendix). These results suggest that the microstructure of 7449 +Cr hinders H diffusivity, while that of 7449 +Ag addition has an opposite effect.

3.4. HEAC behavior under constant mechanical load

The tensile properties (in T76 condition) determined prior to the CL-HEAC test varied, especially for the Ag modified alloy. A tensile strength (σ_m) of 484 ± 19, 477 ± 18 and 451 ± 13 MPa were determined in 7449, 7449 +Cr and 7449 +Ag, respectively. A similar trend was equally observed in the yield strength ($\sigma_{0.2}$), were 468 ± 8, 463 ± 6 and

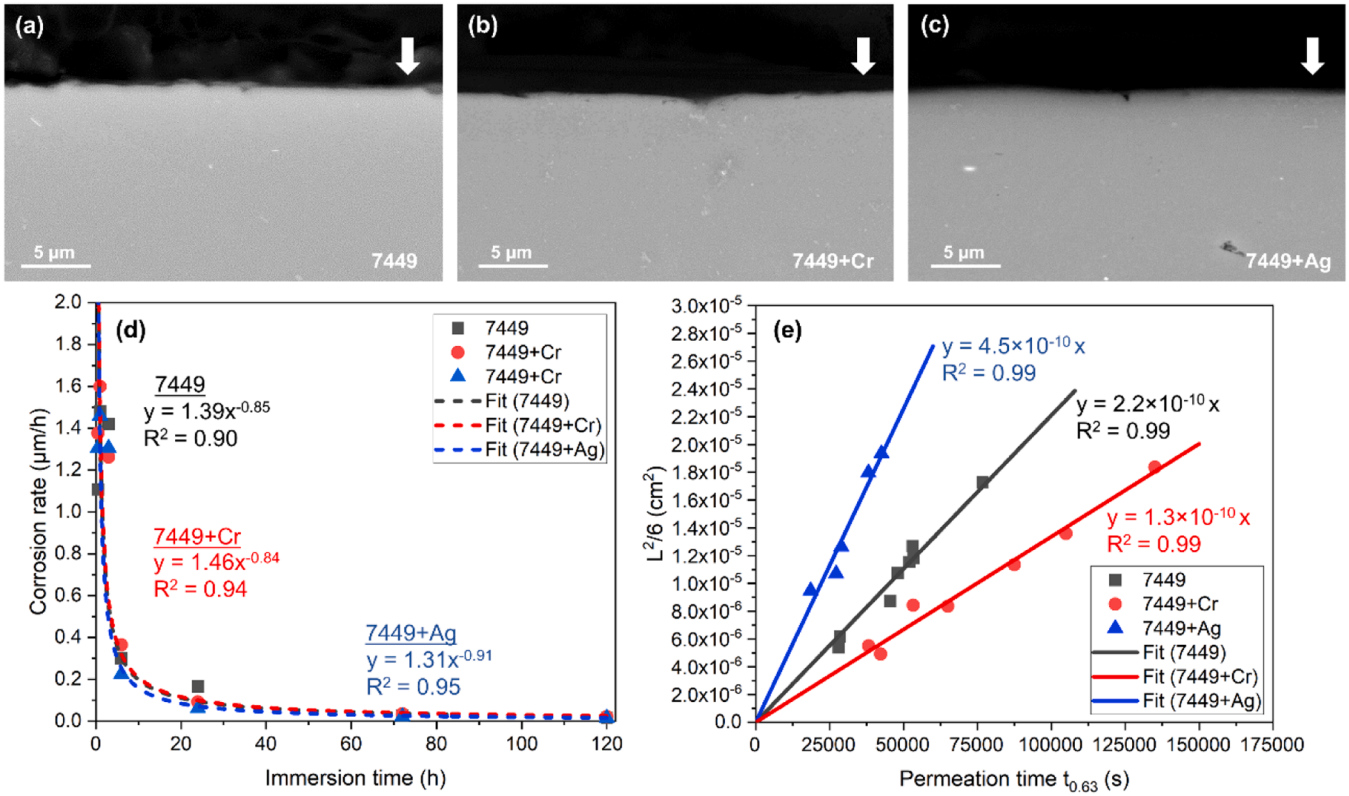

Fig. 8. (a) – (c) SEM-BSE images of alloys after 24 h immersion in 0.01 M NaOH (d) Plot of corrosion rate versus immersion time (e) Plot of $L^2/6$ versus permeation time ($t_{0.63}$) with slope = D_H.

441 ± 9 MPa were determined for 7449, 7449 +Cr and 7449 +Ag, respectively. No strong decrease in strength was observed in the Cr modified alloy relative to the base alloy. In fact, only a 1.5 % decrease in σ_m and only a 1 % decrease in $\sigma_{0.2}$ relative to the base alloy was observed with 0.1 wt% Cr addition, suggesting no significant impact of quench sensitivity on mechanical properties of 7449 plate with a thickness of 70 mm. However, Ag addition resulted in up to 6.8 % decrease in σ_m and a 5.8 % decrease in $\sigma_{0.2}$ compared with the base alloy.

The results of the constant load hydrogen environmentally assisted cracking (CL-HEAC) tests are shown in Fig. 9. The box plots represent the results of 9 tests for 7449 and 7449 +Cr, and 10 tests for 7449 +Ag, while the values on the plots indicate the average lifetime and standard deviation. An average HEAC lifetime of 44 ± 19 days was determined in the 7449 alloy, which slightly decreased to 40 ± 18 days after Ag addition and then increased significantly to 67 ± 19 days with Cr addition. Based on this, it is clear that Ag addition in 7449 has no strong influence on HEAC resistance, as indicated by the marginal decrease in the HEAC lifetime by 4 days. On the other hand, Cr addition enhances the HEAC resistance of 7449, as shown by the 23 days (52 %) increase in the HEAC lifetime in 7449 +Cr relative to 7449.

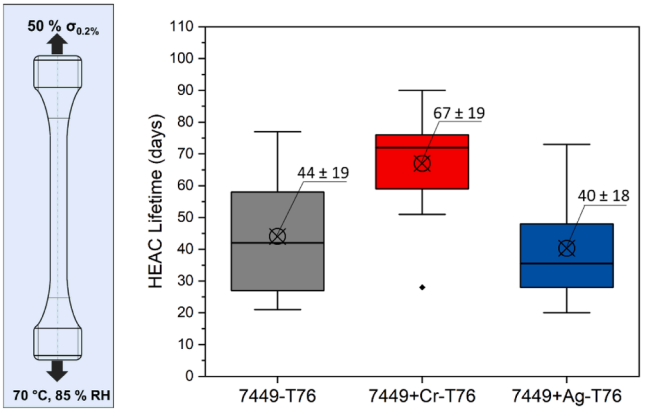

Fig. 9. CL-HEAC test results showing the influence of Cr and Ag on the HEAC lifetime of 7449.

3.5. HEAC fracture surfaces and crack initiation sites

Fig. 10 shows examples of the SEM-SE images of the fracture surfaces, highlighting key features after the CL-HEAC tests. The red-dashed lines in the overview images in Fig. 10 (a), (d) and (g) for 7449, 7449 +Cr and 7449 +Ag, respectively, represent the HEAC fracture plane, which is followed by the region of ductile overload fracture in the center of the samples. The blue boxes show the enlarged region in Fig. 10 (b), (e) and (h) for 7449, 7449 +Cr and 7449 +Ag, respectively. The fracture mode in this region appeared to be mainly intergranular (IG). Some of the numerous proposed HEAC initiation sites at the sample rim-zone are highlighted by the small triangles, while the red boxes show the enlarged portions in Fig. 10 (c), (f) and (i) for 7449, 7449 +Cr and 7449 +Ag, respectively. Clusters of surface-linked IMPs, sometimes associated with pores (Fig. 10 (f), (i)), can be seen at the initiation sites at the sample edges. The clearly defined smooth grain facets confirm that the fracture mechanism is predominantly IG-HEAC with no residual ductility (brittle fracture). The fracture surface appeared relatively clean with no sign of significant oxidation. The observed sites of minor oxidation close to the IMPs cluster could have resulted from exposure of the fracture surface in humid air in the climate chamber or during storage prior to the SEM fracture surface analysis.

Fig. 11(a) – (d) show regions of intergranular (IG)-HEAC at higher magnification. Series of regularly separated CAMs were observed on the fracture surfaces, which strongly suggest a discontinuous crack propagation during the brittle HEAC process.

In addition to IG-HEAC, islands of cleavage-like transgranular (TG)

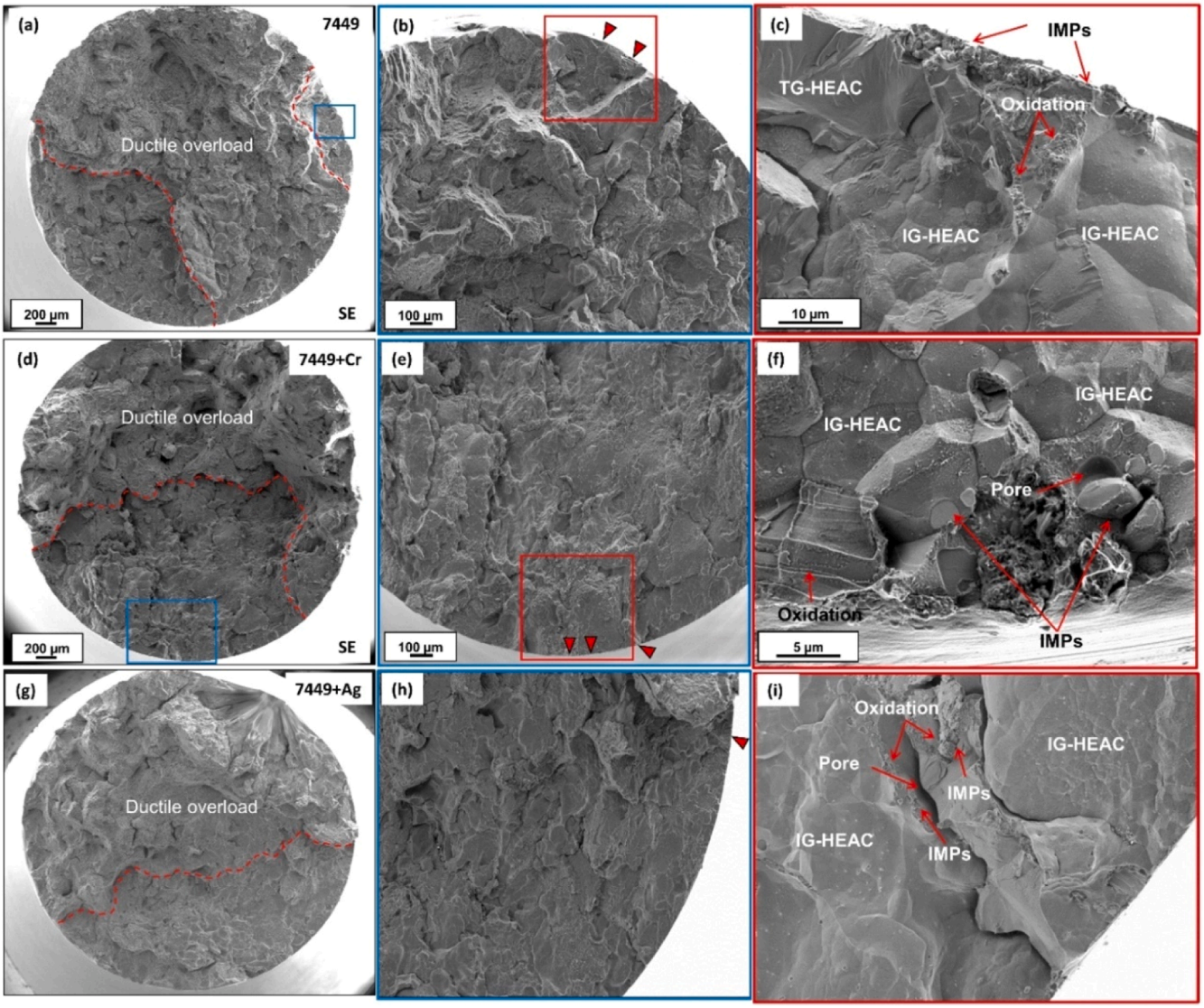

Fig. 10. Overview of fracture surfaces showing the fracture plane (red-dashed lines) and the corresponding region of HEAC fracture (blue boxes) showing the initiation sites (red triangles) and fracture mechanism (red boxes) for 7449 (a) – (c), 7449 +Cr (d) – (f) and 7449 +Ag (g) – (i). For interpretation of the references to color in this figure legend, the reader is referred to the web version of this article.

HEAC were also occasionally observed close to the rim-zone where the cracks originated from. Fig. 10 (c) shows an example of TG-HEAC close to the sample edge, where they appear adjacent to the IG-HEAC. Other regions of crack initiation, where TG-HEAC was equally observed close to the sample rim zone extending ~ 50–100 µm into the fracture surface, followed by IG-HEAC are shown in Fig. 12. TG-HEAC close to the rim zone originated from the large clusters of IMPs, which again were often associated with pores as shown in Fig. 12 (b) – (d). Cleavage-like TG fracture mode during H induced failure can occur under severe loading conditions, which could result from crack tip strain rate under dynamic loading or from the grain shape [9,13]. Such severe conditions are achievable under static loading conditions at the interface of IMPs or at pores, which act as stress raisers [13]. Transition of IG-HEAC to TG-HEAC is observed in 7xxx alloys due to high stress intensity factor (K_I) [5,18]. The occasional occurrence of TG-HEAC close to the rim zone before the on-set of IG-HEAC is likely due to a lack of favorably IG pathway, coupled with hydrogen trapping at the Al/strengthening matrix precipitate interface resulting in interfacial decohesion by HEDE [31,37]. Also, the presence of CAMs on the regions of TG-HEAC shown in Fig. 12 (b) and (c) indicates a discontinuous crack propagation by H embrittlement.

The SEM and the corresponding EDX element maps in Fig. 13 confirm the coarse IMPs cluster at the initiation sites to be Mg_2Si and Al_7Cu_2Fe clusters. The EDX map of oxygen shows oxidation in the vicinity of the initiation sites, which was not only observed directly at the IMPs, but also in areas of the surrounding matrix. However, this is not surprising given the high reactivity of the coarse Mg_2Si phase and the GB $Mg(Zn,Cu,Al)_2$ precipitates due to their high Mg content. Therefore, exposure of the fracture surfaces to humid air after HEAC would result in such surface oxidation. Nano-sized precipitates, such as the E dispersoids in 7449 +Cr and the Ag-rich AlAgZnMgCu phase reported in a different work in 7449 +Ag [44] were not observed on the fracture surfaces due to the resolution limit of the SEM. However, they likely do not play a significant role in HEAC crack initiation in humid air, since nano-sized dispersed particles are highly incapable of sustaining the necessary high stress concentration for initiation.

The SEM images of the sample gauge length close to the fracture surfaces are shown in Fig. 14 (a) – (c). Several secondary cracks (red arrows) were observed, which appeared to be aligned possibly in the longitudinal (L) direction. This points to the fact that the HEAC fracture is likely due to the coalescence of multiple cracks, thus explaining the presence of multiple initiation sites. Bands of plasticity (yellow arrows in

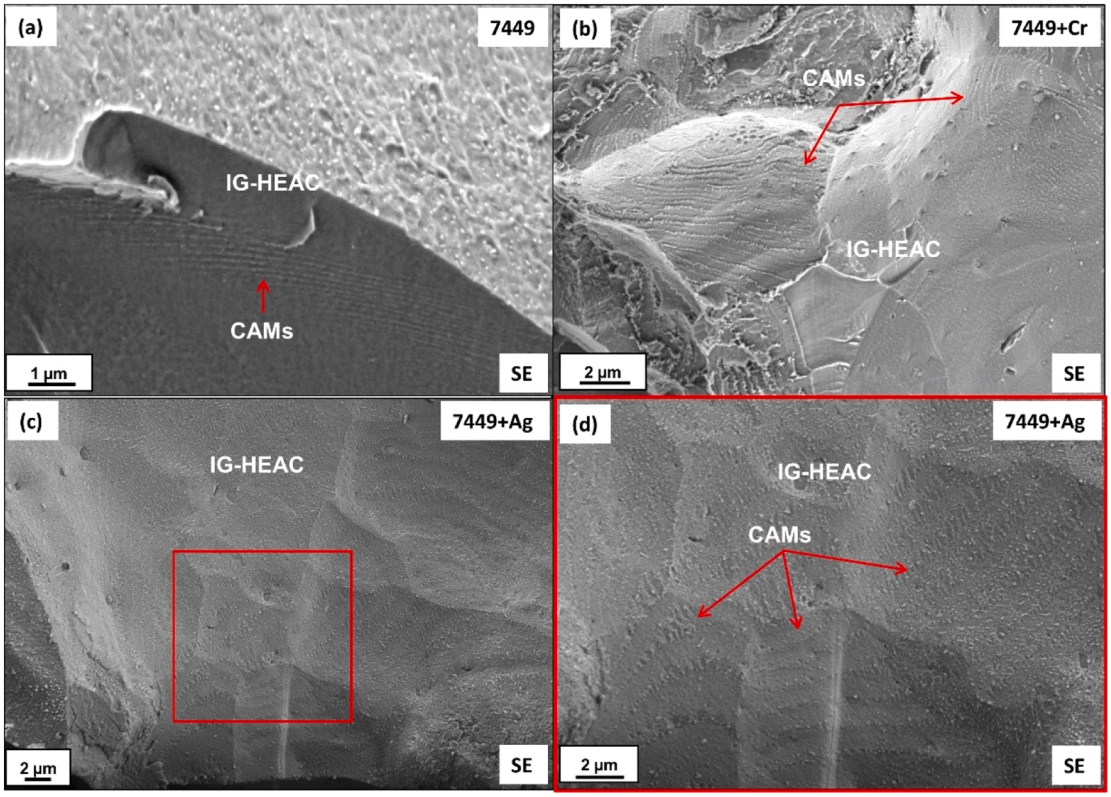

Fig. 11. Regions of intergranular (IG)-HEAC showing CAMs in 7449 (a), 7449 +Cr (b) and 7449 +Ag (c). The red box is shown at higher magnification in (d).

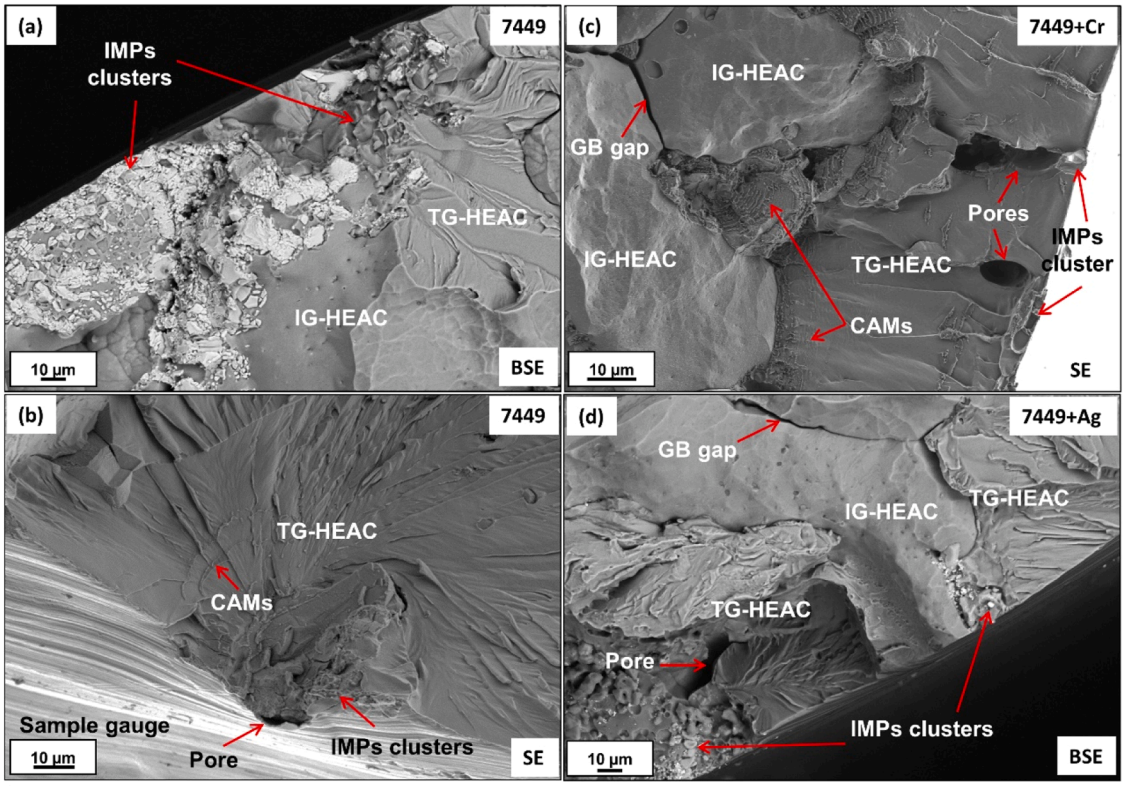

Fig. 12. Regions of TG-HEAC associated with coarse IMPs cluster and pores close to the rim zone for 7449 (a) – (b), 7449 +Cr (c) and 7449 +Ag (d).

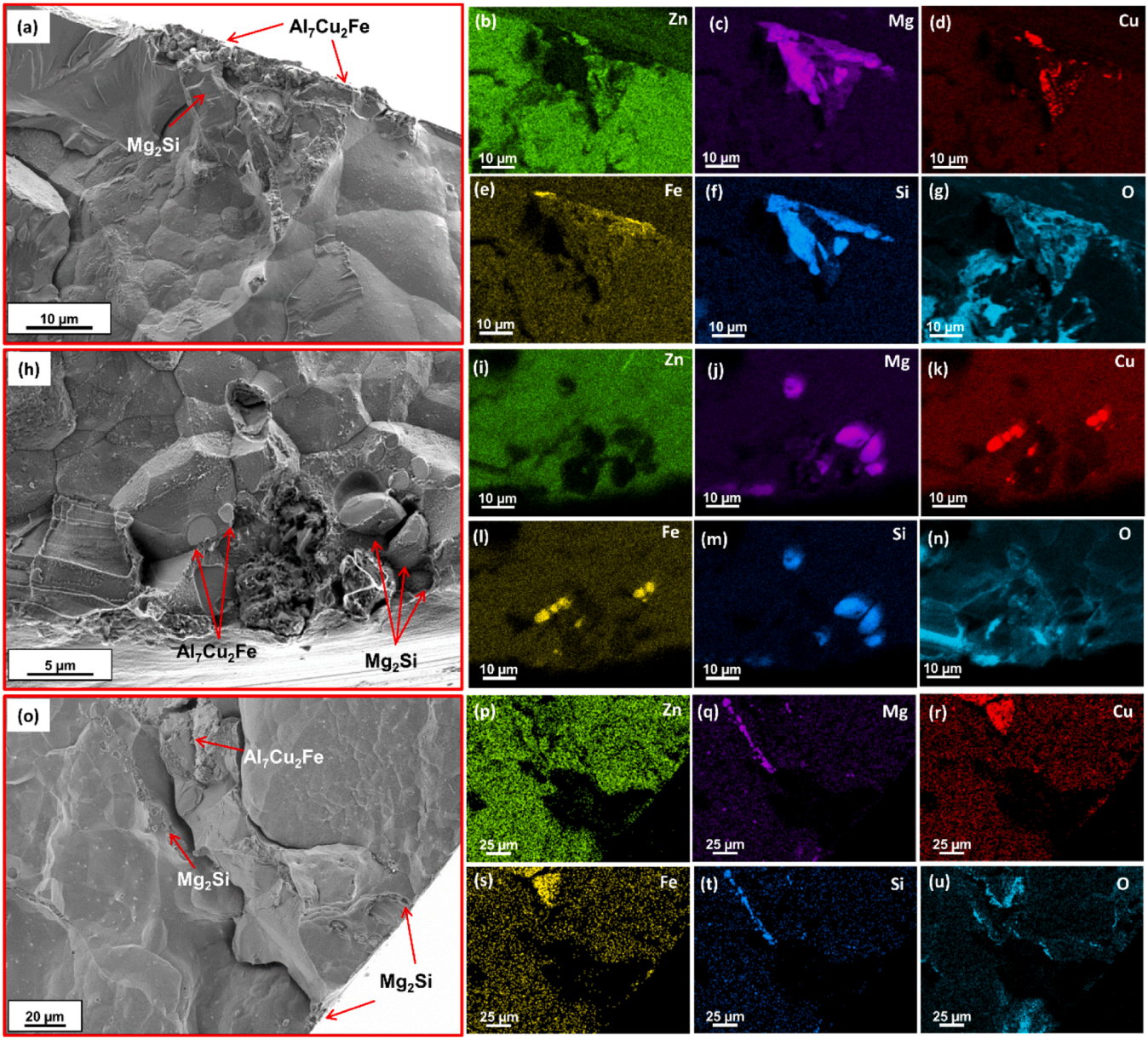

Fig. 13. SEM images and the corresponding EDX element maps of the initiation sites showing coarse Al_7Cu_2Fe and Mg2Si IMP clusters (a) – (g) 7449 (h) – (n) 7449 +Cr and (o) – (u) 7449 +Ag.

Fig. 14 (b)) were also observed in the vicinity of the micro-cracks. The red box in Fig. 14 (a) is shown in Fig. 14 (d). The corresponding EDX element maps in Fig. 14 (e) – (j) show that these secondary cracks initiated at the coarse IMPs and then propagated by splitting the particles (Al_7Cu_2Fe in this case) before they stopped growing. These observations further confirm that HEAC initiation in these alloys occur in the vicinity of intermetallic particles (IMP) clusters linked to the sample surface, which act as stress raisers under mechanical load [5,18,19,22]. The oxygen EDX map (Fig. 14 (j)) also shows evidence of oxidation localized at the IMPs, particularly on the high Mg-containing (coarse) Mg_2Si phase.

4. Discussion

4.1. Influence of Cr and Ag on grain boundary (GB) microstructure and microchemistry

Grain boundary (GB) microstructure and microchemistry have a strong influence on the properties of 7xxx alloys. While Cr addition in 7xxx alloys controls recrystallization and grain growth through the formation of E dispersoids [4,55,58,59], Ag is added to enhance the matrix precipitation kinetics which affects the precipitate area coverage adjacent to the GBs and the precipitate free zone (PFZ) width [42,60,61]. However, both alloying additions can directly or indirectly affect the GB microstructure and microchemistry, as shown in this study. Two families of grain boundary η $Mg(Zn,Cu,Al)_2$ precipitates (GBP), namely, quench-induced (Q-GBP) and aging-induced (A-GBP) precipitates have been reported in commercial 7xxx thick plates [6]. The former is formed during quenching from solution heat treatment temperature, due to decreasing cooling rate (temperature gradient) from the plate edge to the centre position. The latter are formed during artificial aging due to the high interface energy of GBs. These families of GBP in 7xxx alloys differ in terms of size and composition, both of which are influenced by alloy chemistry (Zn+Mg+Cu) [6,62]. For example, in 7050 alloy, the Q-GBP are large with a complex dendritic morphology and contains a higher amount of Cu than the A-GBP due to their higher nucleation

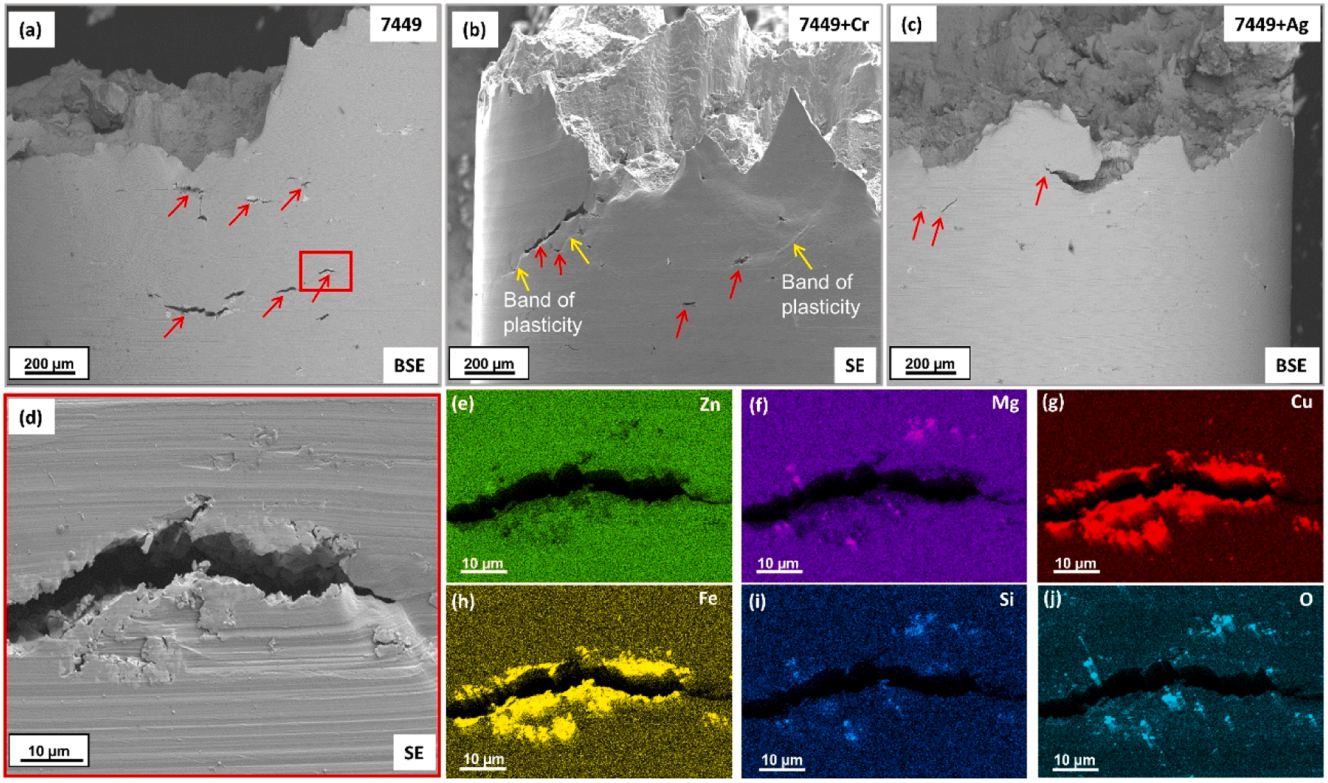

Fig. 14. (a) – (c) SEM images of the sample gauge showing secondary short cracks along the L-direction. (d) Enlarged portion indicated by red box in (a) and the corresponding EDX element maps (e) – (j). For interpretation of the references to color in this figure legend, the reader is referred to the web version of this article.

temperature [6]. Since differentiating these families of GBP was not a direct focus of this study, the GBPs size and chemistry reported in this study are a combination of both precipitate types. However, due to their crucial role on HEAC, only precipitation on HAGBs were investigated.

During ingot solidification, Cr segregates from the grain center towards the GBs [59]. This results in E dispersoid formation adjacent to the GBs or even at the GBs (Fig. 4(e) and 6 (a)), during homogenization. The E phase is relatively large in size (compared to other dispersoids like Al_3Zr), incoherent with Al-matrix and induces quench sensitivity by heterogeneous nucleation of large η $Mg(Zn,Cu,Al)_2$ at E/Al interface [40, 55]. These heterogeneously nucleated η $Mg(Zn,Cu,Al)_2$ phase can be likened to the Q-GBP, since they are formed during quenching from SHT [40]. This would mean that the fraction of Q-GBP will be highest in 7449 +Cr due to the presence of E dispersoids adjacent to or at the GBs. Moreover, the quench sensitive E phase equally dissolves ~ 3.9 at% Cu and ~ 4.5 at% Zn after solution treatment [63]. Therefore, their presence in 7xxx alloys depletes vacancies and solutes (Mg, Zn, Cu) diffusing to the GBs where they are annihilated or partition/form precipitates, respectively, during artificial aging [64]. The current results show that the E dispersoids formation has an effect on the GB microstructural features observed in 7449 +Cr with respect to the reference alloy as reported in Table 2. The depletion of solute atoms due to E phase formation and the precipitation and growth of the large Q-GBP will essentially lower the fraction of the small A-GBP formed during artificial aging in 7449 +Cr or the growth of Q-GBP, particularly in the vicinity of the E dispersoids. Subsequent growth of the quench-induced η $Mg(Zn,Cu,Al)_2$ at the E/Al interface not only results in a wider PFZ formation, but also explains the higher GBP spacing in the 7449 +Cr alloy relative to the base (7449) alloy. The impact of Cr addition equally reflects on the GBP chemistry shown in Table 3, were a higher Cu content was determined by STEM-EDX in the GBPs in 7449 +Cr compared to the reference alloy. However, the GBP probed by APT are likely the A-GBP variant, due to their relatively smaller size, and, therefore explains the difference in composition with the STEM-EDX results. Considering the high sampling statistics of the STEM-EDX measurements for the Cliff Lorimer (CL) extrapolation, the reported results in Table 3 would be a better representation of the GBP chemistry.

Alteration of the type/morphology and chemistry of the matrix and grain boundary (GB) precipitates, respectively, in 7xxx alloys equally occurs with Ag addition [41,44,65]. Ag is believed to enhance nano-sized strengthening phase precipitation in the grain interior and adjacent to the grain boundaries, which essentially suppresses PFZ formation. Solutes and mainly vacancy depletion due to their migration from the adjacent matrix to the GBs during quenching is the mechanism of PFZ formation in 7xxx alloys [42,61,66]. This effect of PFZ suppression by Ag is due to the strong binding energy of Ag with vacancy and solute atoms [42,61,67], which limits their diffusion to the GBs. Suppressed solute migration to the GBs not only favors fine GP zones and η' formation in the matrix [65], but equally suppresses GB precipitation and growth during artificial aging [41]. Notwithstanding, the aforementioned effects of Ag has mainly been observed in Cu-free 7xxx variants, with a Zn/Mg ratio of ~ 2. Referring to the results in Table 2, Ag addition only marginally reduced the size of the GBP, the GBP spacing and the PFZ width on a HAGB relative to the base alloy. This negligible effect of Ag on the PFZ width corroborates the result of a recent work on an Al-Zn-Mg-Cu-Zr alloy with a Zn/Mg ratio of 4 [44]. However, Wang et al. [65] in a study observed up to 50 % decrease in the PFZ width with 0.3 wt% Ag addition in 7075 after peak aging. But, it wasn't specified if the investigated PFZ widths on the 7075 and 7075 +Ag alloys were on a similar type of GB, which is important to consider, since precipitation on a high and low angle GB differ in terms of size, morphology and the adjacent PFZ width, due to GB orientation [68]. Regarding the role of Ag on the GB micro-chemistry, only ~ 1 at% Ag dissolves in the GB η $Mg(Zn,Cu,Al)_2$ phase in 7449 +Ag and segregation of Ag at the GBs does not occur in 7xxx alloy [44].

4.2. Hydrogen diffusion and trapping with of Cr and Ag addition in 7449

H permeability is strongly influenced by the alloy chemistry and processing-induced microstructural features, which act as quasi-permanent (irreversible) or temporary (reversible) H trap sites during H permeation measurements [69–71]. Therefore, effective H diffusion is faster in commercially pure 1xxx alloy like 1060 than in a commercial 7xxx alloy like 7075 [72]. GBs are believed to be the preferred diffusion path for H in FCC metals like Al alloys [70,73]. The GBs area per unit volume and the presence of GBPs affects H transport in the microstructure of 7xxx alloys during permeation measurements [31,74]. According to the microstructure characterization results in Fig. 3, 7449 +Ag had the smallest grain size and the highest fraction of HAGBs relative to 7449 and 7449 +Cr. Since H diffusion is accelerated at HAGB [75], this means that the H entry and diffusion path density will be highest in 7449 +Ag, and therefore explains the enhanced H transport in the microstructure. Nevertheless, the role of H trapping at defects should also be taken into consideration, since reversible or irreversible traps hinder H diffusion [49]. Notable trap sites in 7xxx alloys include vacancies [31,74], dislocations [70], HAGBs [31,32,76], coarse intermetallic particles [31,32,36], dispersoids [32,36,39] and the interface of η/Al matrix [77].

Density functional theory (DFT) calculations of H trapping energy shown in Table 4 suggests that high H trapping capacity is achievable at microstructural features with a high trapping energy per H atom. According to the H partitioning principle, H entering a 7xxx alloy first accumulates at defects with a high trapping energy [31,32,36]. Based on this, absorbed H during permeation test in these alloys will first partition in the interior of Al_7Cu_2Fe, followed by that of E-$Al_{18}Mg_3Cr_2$ (7449 +Cr), and then at η/Al interface, before diffusing/partitioning along the GBs.

Since a similar primary phase fraction was determined as shown in Fig. 3(a) – (c), the delayed hydrogen permeability and the decreased effective H diffusion coefficient (D_H) in 7449 +Cr, relative to 7449, is influenced by the E dispersoids with a high trapping energy. Furthermore, D_H in 7449 +Cr is also affected by H trapping at the E/Al matrix interface [39], the large quench-induced η-$MgZn_2$/Al-matrix interface and at dislocations due to stored energy [76,80]. Despite the reported low DFT trapping energy of dislocations, experimental studies have shown significant H trapping at dislocations [76,80]. Bhuiyan et al. [76,81] reported that dislocations have a high trap site occupancy than GBs in high H environment. Therefore, H trapping at dislocations during permeation at high H fugacity will be slightly higher and lower (with respect to the base alloy) in 7449 +Cr and 7449 +Ag, respectively. Considering these microstructural features, it is plausible to concluded that a combination of H trapping at the E dispersoids and at dislocations due to stored energy is responsible for the lower D_H in 7449 +Cr relative to the 7449 alloy. For the Ag-modified alloy, the higher D_H relative to reference alloy can be explained by the higher density of H diffusion paths and the lowest trap site density, presumably due to a lower dislocation density. A model of the role of Cr and Ag on H diffusivity in 7449 alloy during permeation measurements is schematically illustrated in Fig. 15. Due to a comparable primary phase fraction (PF) in the alloys (Fig. 3(a) – (c)), H trapping at coarse Al_7Cu_2Fe are assumed to be the same in the alloys, and therefore excluded from the model in Fig. 15.

Table 4
DFT trapping energy of common defects/microstructural features in 7xxx alloys.

Defect/microstructural feature	Trapping energy (eV.H^{-1})	Reference
Mg_2Si	− 0.2	[32]
η-$MgZn_2$	0.08	[31,78]
Al_3Zr ($L1_2$)	0.12	[32]
Dislocation (edge)	0.17	[31,32]
Grain boundary	0.20 – 0.27	[31,32,79]
η-$MgZn_2$/Al interface	0.32	[31,78]
E-$Al_{18}Mg_3Cr_2$	0.37	[32]
Al_7Cu_2Fe	0.56	[32]

4.3. Mechanistic understanding of the influence of Cr and Ag on HEAC

H – microstructure interaction in 7xxx alloys is crucial in elucidating the HEAC mechanism [9,32,36,72]. In humid air, there is a lack of extensive corrosion like pitting or IGC that form critical defects for crack initiation. Nonetheless, in-situ measurements [17,19,21,22] have shown coarse IMPs/Al-matrix interfaces, metal ligaments connecting surface-linked pores and GBs of Rex grains to be the common initiation sites for HEAC in warm humid air. The HEAC fracture surfaces in Fig. 13 showed the clusters of Al_7Cu_2Fe and Mg_2Si, sometimes associated with pores at the initiation sites. These sites are prone to defect formation during processing (hot rolling) or mechanical loading, due to non-uniform deformation. Referencing the proposed stages of HEAC after exposure to humid air [20,21], alteration of the surface conditions, local chemical activities and stress states occur at these occluded defects. Although re-passivation at these sites is inevitable, the formation of a disordered liquid-like layer occurs above 70 % RH at the oxide surface [11,25,69]. This could penetrate through the weakened or altered oxide/hydroxide layer, thus, providing the needed electrolyte to drive local chemical activity at the oxide/metal interface. Moreover, condensation at these occluded sites will promote local Al-matrix oxidation, selective oxidation of Mg in the Mg_2Si phase and/or the partial dissolution of the GB η $Mg(Zn,Cu,Al)_2$ phase. This facilitates the concomitant production of H by water reduction at cathodic sites like the Al_7Cu_2Fe particles, which is an essential part of the HEAC incubation process [16]. Hence, an alloy's microstructure, notably the chemistry of the η $Mg(Zn,Cu,Al)_2$ (which is defined by the alloy chemistry), is relevant for H production for the HEAC process [6,82]. Young and Scully have shown in their work [16,69] that crack growth rate in 7xxx alloys is dependent on the sum of a number of thermally-activated processes, including hydrogen production, adsorption and diffusion. Moreover, overaging a Cu-containing 7xxx alloy decreases the apparent H diffusivity and the stage II (K-independent) crack growth rate, presumably due to increased nobility of the η $Mg(Zn,Cu,Al)_2$ after overaging, resulting from the significant Cu partitioning and decreased H production rate [9,16,34,82]. Therefore, the higher Cu content of the GB η $Mg(Zn,Cu,Al)_2$ phase in 7449 +Cr (Table 3) would essentially lower its reactivity and the concomitant local H production rate in comparison to the base alloy. This is corroborated by the decrease in the intergranular corrosion penetration rate, driven mainly by the dissolution of the GB η $Mg(Zn,Cu,Al)_2$ phase, with minor Cr addition in 7449 reported in a different study [40]. In 7449 +Ag alloy, the incorporation of only ~ 1 at% Ag in the GB η Mg$(Zn,Cu,Al)_2$ phase is likely insufficient to induce a significant impact on its nobility relative to the reference alloy [44]. However, it is unclear to what extent the cathodic Ag-rich AlAgZnMgCu phase in 7449 +Ag alloy [44] can accelerate local cathodic H generation rate in humid air, since only a marginal decrease (by 4 days) in the HEAC lifetime in 7449 +Ag relative to the base alloy was observed by the CL-HEAC test shown in Fig. 9.

The proposed HEAC damage mechanisms (HEDE, HELP and AIDE) in Al alloys entails the diffusion and localization/trapping of the produced H atoms ahead of a crack tip [29,83]. According to Young and Scully [69], HEAC propagation will only occur, when a critical H concentration ahead of a crack tip is exceeded. This is corroborated by the DFT results of Tsuru et al. [31], were a continuous deterioration of the cohesive energy with increasing H occupancy at η/Al interface, was observed. This means that suppressed local H production and diffusivity, coupled with enhanced trapping, preferably in the interior of IMPs, will delay the transition from the incubation stage to the initiation stage (induced by crack tip sharpening) and their transition to sustained propagation. Crack arrest marks (CAMs) on the fracture surfaces (Fig. 11) are indicative of a discontinuous HEAC propagation, driven by the intermittent H supply during the process [83]. Therefore, for cracks to continue to propagate in humid air, regular supply of H ahead of a crack tip to

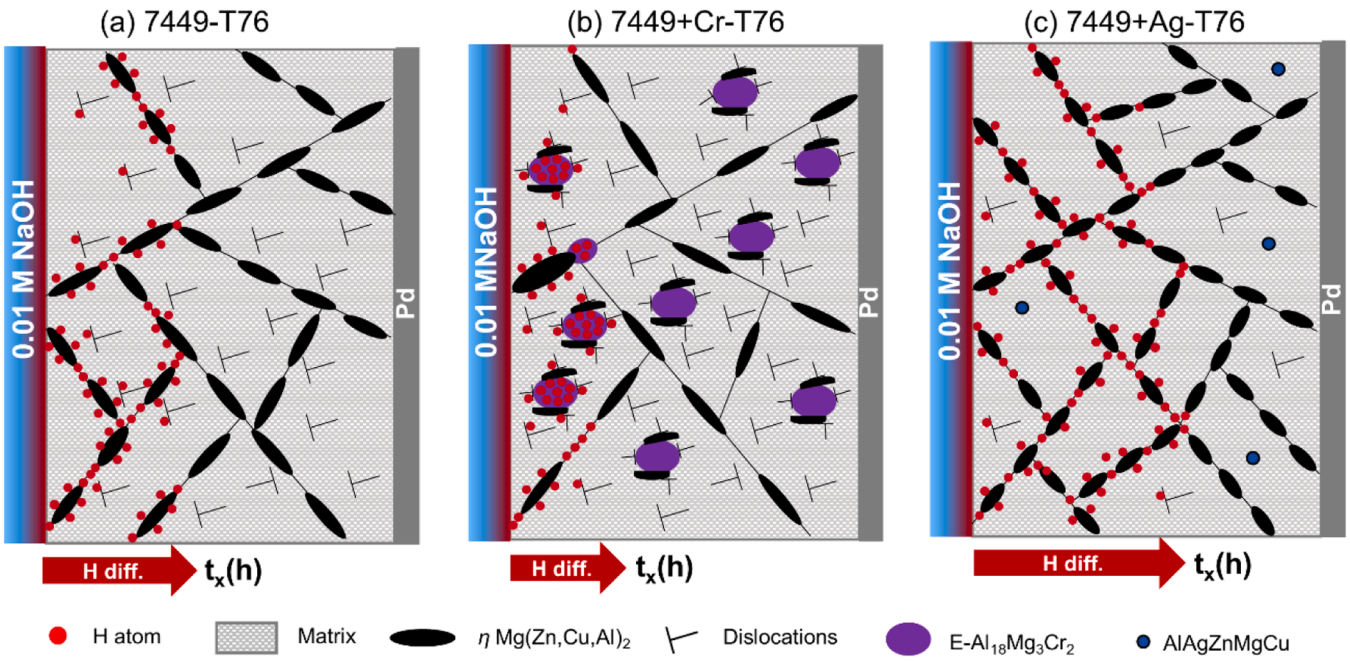

Fig. 15. Schematic illustration of the role of Cr and Ag on H diffusivity and trapping in 7449.

achieve this threshold is necessary. The increased H trapping capacity of 7449 +Cr due to the presence of the E-dispersoids with a high interior trapping energy (second to Al_7Cu_2Fe), as shown by the permeation results (Fig. 8), will delay the time to reach this critical H concentration at the GBs and the η/Al interface ahead of a crack tip, which will only occur upon saturation of Al_7Cu_2Fe clusters and the E-dispersoids [32,36,37]. This is believed to contribute to the improvement in the HEAC resistance in the Cr-modified alloy. Once this threshold is reached and exceeded, H-induced damage will occur, probably by the weakening of the cohesive bond (Hydrogen Enhanced Decohesion) at the grain boundaries (GBs) or η/Al interfaces [31,36].

Another important consideration for the mechanistic understanding of HEAC mechanism in 7xxx alloys is solute segregation at the GBs and the PFZ width. The soft PFZ, which is prone to preferential slip, and free Zn and Mg (unbound in precipitates) at the GBs have been proposed to influence the susceptibility of a GB to SCC and HEAC [9,34,36]. The precise role of PFZ width remain unclear since 7449 +Cr alloy with the highest PFZ width shows a better HEAC resistance than 7449 and 7449 +Ag with smaller PFZ widths. Regarding GB segregation, while a linear relationship between GB Zn content and the SCC time-to-fracture has been reported [84], the role of GB Mg segregation remains controversial [12,85]. However, it is believed that the presence of these active elements at the GBs could facilitate H entry into the microstructure, even though this might not necessarily be the main controlling factor for HEAC susceptibility [11]. Zhao et al. [36] recently reported that although H uptake at the GB is not necessarily promoted by Mg segregation, co-segregation of Mg and H at the GB enhances GB embrittlement by decohesion. It was hypothesized that the elimination of free Mg at the GBs could be beneficial in suppressing HEAC. Since the E-Al$_{18}$Mg$_3$Cr$_2$ phase in 7449 +Cr contains up to ~ 12 at% Mg [55], its formation possibly hinders free solute diffusion to the GBs and, therefore, accounts for the lower free Mg at the GB in 7449 +Cr (0.75 at%) relative to the 7449 alloy (2.03 at%), shown in Fig. 5. But again, the measured GB segregation level of Mg in 7449 +Ag (0.81 at%) is

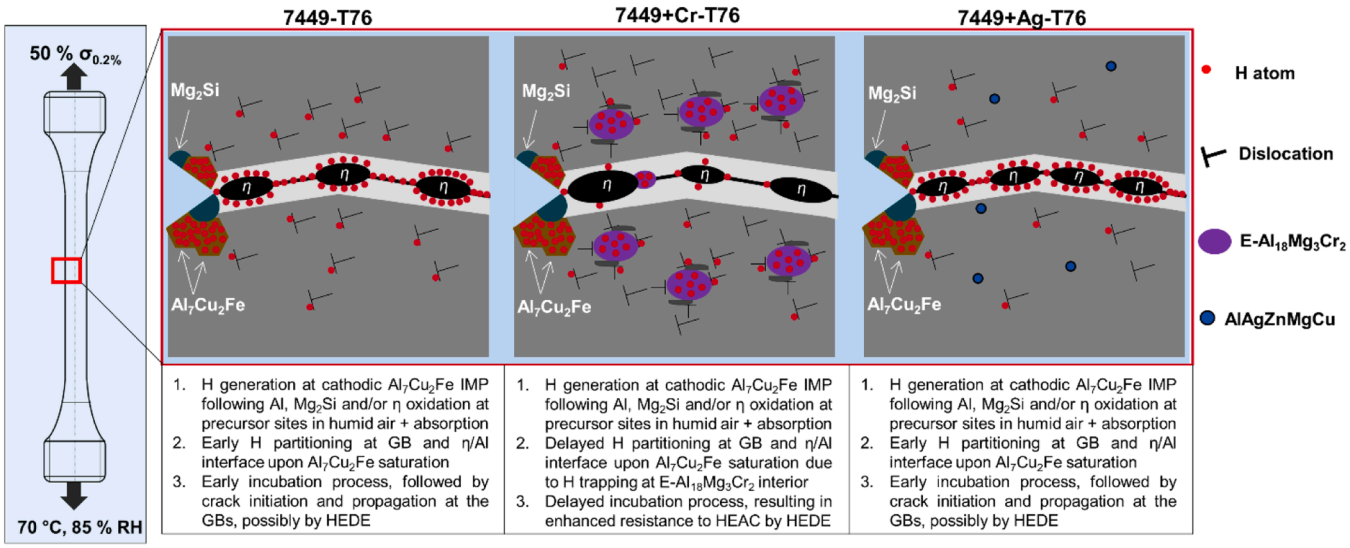

Fig. 16. Schematic diagram of the role of Cr and Ag addition on the HEAC mechanism of 7449.

comparable to that of 7449 +Cr alloy, suggesting that the strong binding energy of Ag to solutes presumably suppresses GB Mg solute migration. Nonetheless, given the marginal difference in the HEAC lifetime of 7449 and 7449 +Ag, it is unlikely that the minor GB segregation, alone, is the main driving force for HEAC. The trap site density and probably the chemistry of the GBP are believed to have a dominant effect on the HEAC susceptibility of these alloys. Based on these results, a schematic illustration of the role of Cr and Ag on the HEAC mechanism of 7449 alloy is presented in Fig. 16.

5. Conclusion

This study explored a potential HEAC suppression approach in a new generation 7xxx alloy through alloy chemistry modification by minor Cr and Ag additions. Based on the GB microstructure/chemistry, H permeability, time-to-failure under constant load HEAC test and the analysis of the fracture surfaces, the following can be concluded.

1. The average GB coverage by precipitates decreases with 0.1 wt% Cr and 0.3 wt% Ag addition in 7449 owing to the formation of the quench sensitive E-$Al_{18}Mg_3Cr_2$ dispersoid and the strong binding energy of Ag with solutes and vacancies in the matrix, respectively.
2. Minor Cr addition in 7449 enhances the formation of quench-induced η $Mg(Zn,Cu,Al)_2$ phase, with a higher Cu content of up to 15 at%.
3. Minor Ag addition in 7449 does not significantly reduce the PFZ width and only $\sim$ 1 at% Ag dissolves in the GBP precipitate.
4. Minor Cr addition in 7449 increases the H trap site density mainly due to the formation of E-$Al_{18}Mg_3Cr_2$ dispersoids with a high trapping energy. H trapping in the E-$Al_{18}Mg_3Cr_2$ interior, in addition to a less reactive GB microchemistry enhanced the HEAC resistance in humid air (70 °C, 85 % RH) by increasing the average time-to-failure by up to 50 %, precisely from 44 $\pm$ 19 days in 7449–67 $\pm$ 19 days in 7449 +Cr.
5. Minor Ag addition in 7449 has little to no effect on the HEAC resistance in humid air, with the average time-to-failure (days) only decreasing marginally from 44 $\pm$ 19 to 40 $\pm$ 18.
6. Minor Cr and Ag addition does not alter the HEAC fracture mode, with both the base alloy and the modified alloys showing discontinuous IG-HEAC and TG-HEAC fracture.

CRediT authorship contribution statement

Akuata Chijioke Kenneth: Writing – review & editing, Writing – original draft, Methodology, Investigation, Formal analysis, Data curation, Conceptualization. **Belkacemi Lisa T.:** Writing – review & editing, Investigation. **Beyß Oliver:** Writing – review & editing, Methodology. **Curd Matthew E.:** Investigation. **Hantzsche Kerstin:** Investigation. **Zander Daniela:** Writing – review & editing, Supervision, Project administration, Funding acquisition, Conceptualization.

Declaration of Competing Interest

The authors declare that they have no known competing financial interests or personal relationships that could have appeared to influence the work reported in this paper

Acknowledgements

The technical support of Martina Thoennissen, Stefanie Düker, and Elke Schaberger-Zimmermann is greatly appreciated. We gratefully acknowledge the Ph.D. funding of Chijioke Kenneth Akuata granted under the Guidelines for the Promotion of Young Academics (RFwN) of the RWTH Aachen University and the support of the Airbus Advanced Metal Research Program (AMRP).

Appendices

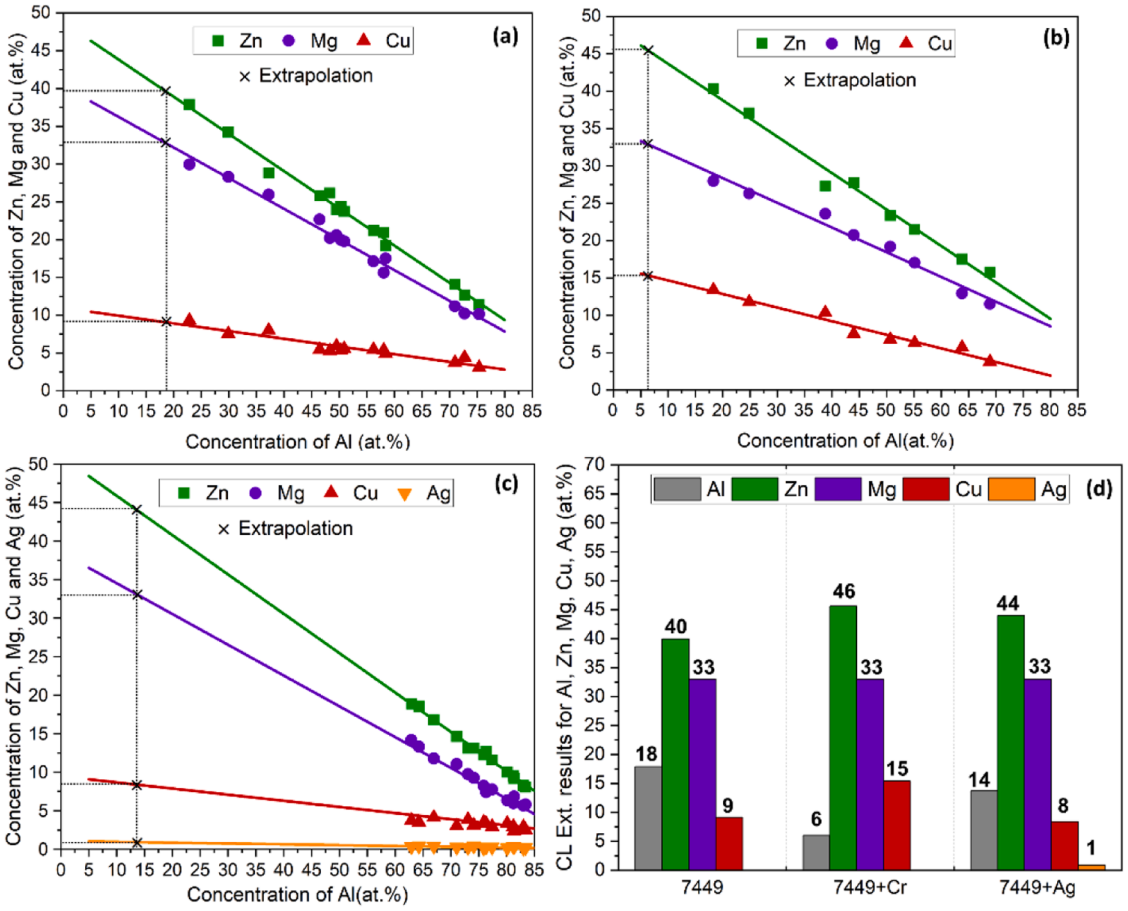

Figure A.1. Cliff lorimer (CL) extrapolation (a) 7449 (b)7449 +Cr (c) 7449 +Ag. The plot of the extrapolation results shown in Table 3 is shown in (d)

Table A.1
Summary of D_H determined for five different membrane thicknesses in each alloy

Alloy (T76)	L (μm)	D_H (cm^2/s)	Average D_H (cm^2/s)
7449	59	1.92×10^{-10}	$2.11 (\pm 0.17) \times 10^{-10}$
	75	1.92×10^{-10}	
	83	2.24×10^{-10}	
	87	2.21×10^{-10}	
	105	2.25×10^{-10}	
7449 +Cr	57	1.16×10^{-10}	$1.31 (\pm 0.10) \times 10^{-10}$
	60	1.44×10^{-10}	
	74	1.29×10^{-10}	
	86	1.30×10^{-10}	
	109	1.36×10^{-10}	
7449 +Ag	77	5.10×10^{-10}	$4.53 (\pm 0.43) \times 10^{-10}$
	82	3.93×10^{-10}	
	89	4.36×10^{-10}	
	106	4.72×10^{-10}	
	110	4.55×10^{-10}	

Data availability

The data that has been used is confidential.

References

[1] N.J.H. Holroyd, T.L. Burnett, J.J. Lewandowski, G.M. Scamans, Environment-induced cracking of high-strength Al-Zn-Mg-Cu aluminum alloys: past, present, and future, Corrosion 79 (2022) 48–71, https://doi.org/10.5006/4149.
[2] T. Dursun, C. Soutis, Recent developments in advanced aircraft aluminium alloys, Mater. Des. 56 (1980-2015) (2014) 862–871, https://doi.org/10.1016/j.matdes.2013.12.002.

[3] X. Zhang, Y. Chen, J. Hu, Recent advances in the development of aerospace materials, Prog. Aerosp. Sci. 97 (2018) 22–34, https://doi.org/10.1016/j.paerosci.2018.01.001.

[4] M. Conserva, E. Di Russo, O. Caloni, Comparison of the influence of chromium and zirconium on the quench sensitivity of Al-Zn-Mg-Cu alloys, Metall. Trans. 2 (1971) 1227–1232, https://doi.org/10.1007/BF02664256.

[5] E. Schwarzenböck, E. Ollivier, A. Garner, A. Cassell, T. Hack, Z. Barrett, C. Engel, T. L. Burnett, N.J.H. Holroyd, J.D. Robson, P.B. Prangnell, Environmental cracking performance of new generation thick plate 7000-T7x series alloys in humid air, Corros. Sci. 171 (2020) 108701, https://doi.org/10.1016/j.corsci.2020.108701.

[6] A. Garner, R. Euesden, Y. Yao, Y. Aboura, H. Zhao, J. Donoghue, M. Curioni, B. Gault, P. Shanthraj, Z. Barrett, C. Engel, T.L. Burnett, P.B. Prangnell, Multiscale analysis of grain boundary microstructure in high strength 7xxx Al alloys, Acta Mater. 202 (2021) 190–210, https://doi.org/10.1016/j.actamat.2020.10.021.

[7] U. De Francisco, N.O. Larrosa, M.J. Peel, Hydrogen environmentally assisted cracking during static loading of AA7075 and AA7449, Mater. Sci. Eng.: A 772 (2020) 138662, https://doi.org/10.1016/j.msea.2019.138662.

[8] Environmentally Assisted Cracking in certain Aluminium Alloys, in: European Union Aviation Safety Agency (EASA) - Safety Information Bulletin Airworthiness 2018–04R2.

[9] N.J.H. Holroyd, Environment-Induced Cracking of High-Strength Aluminum Alloys, in: R.P. Gangloff and M.B. Ives Environment-Induced Cracking of Metals NACE, Houston, TX, 1990, pp. 311-345.

[10] M.O. Speidel, Stress corrosion cracking of aluminum alloys, Metall. Trans. A 6 (1975) 631–651, https://doi.org/10.1007/BF02672284.

[11] N.J.H. Holroyd, G.M. Scamans, Crack propagation during sustained-load cracking of Al-Zn-Mg-Cu aluminum alloys exposed to moist air or distilled water, Metall. Mater. Trans. A 42 (2011) 3979–3998, https://doi.org/10.1007/s11661-011-0793-x.

[12] T.D. Burleigh, The postulated mechanisms for stress corrosion cracking of aluminum alloys: a review of the literature 1980-1989, Corrosion 47 (1991) 89–98, https://doi.org/10.5006/1.3585235.

[13] R. Braun, Environmentally assisted cracking of aluminium alloys, Mater. und Werkst. 38 (2007) 674–689, https://doi.org/10.1002/mawe.200700204.

[14] R.G. Song, W. Dietzel, B.J. Zhang, W.J. Liu, M.K. Tseng, A. Atrens, Stress corrosion cracking and hydrogen embrittlement of an Al–Zn–Mg–Cu alloy, Acta Mater. 52 (2004) 4727–4743, https://doi.org/10.1016/j.actamat.2004.06.023.

[15] D. Najjar, T. Magnin, T.J. Warner, Influence of critical surface defects and localized competition between anodic dissolution and hydrogen effects during stress corrosion cracking of a 7050 aluminium alloy, Mater. Sci. Eng.: A 238 (1997) 293–302, https://doi.org/10.1016/S0921-5093(97)00369-9.

[16] G.A. Young, J.R. Scully, The effects of test temperature, temper, and alloyed copper on the hydrogen-controlled crack growth rate of an Al-Zn-Mg-(Cu) alloy, Metall. Mater. Trans. A 33 (2002) 1167–1181, https://doi.org/10.1007/s11661-002-0218-y.

[17] U. De Francisco, F. Beckmann, J. Moosmann, N.O. Larrosa, M.J. Peel, 3D characterisation of hydrogen environmentally assisted cracking during static loading of AA7449-T7651, Int. J. Fract. 232 (2021) 93–116, https://doi.org/10.1007/s10704-021-00595-y.

[18] Y. Aboura, A.J. Garner, R. Euesden, Z. Barrett, C. Engel, N.J.H. Holroyd, P. B. Prangnell, T.L. Burnett, Understanding the environmentally assisted cracking (EAC) initiation and propagation of new generation 7xxx alloys using slow strain rate testing, Corros. Sci. 199 (2022) 110161, https://doi.org/10.1016/j.corsci.2022.110161.

[19] R.T. Euesden, Y. Aboura, A.J. Garner, T. Jailin, C. Grant, Z. Barrett, C. Engel, P. Shanthraj, N.J.H. Holroyd, P.B. Prangnell, T.L. Burnett, In-situ observation of environmentally assisted crack initiation and short crack growth behaviour of new-generation 7xxx series alloys in humid air, Corros. Sci. 216 (2023) 111051, https://doi.org/10.1016/j.corsci.2023.111051.

[20] R.W. Staehle, Quantitative Micro-Nano (QMN) Approach to SCC Mechanism and Prediction-Starting a Third Meeting. in, Springer International Publishing, Cham, 2016, pp. 1535–1629.

[21] V.C. Gudla, M. Storm, B.C. Palmer, J.J. Lewandowski, P.J. Withers, N.J.H. Holroyd, T.L. Burnett, Environmentally induced crack (EIC) initiation, propagation, and failure: a 3D in-situ time-lapse study of AA5083 H131, Corros. Sci. 174 (2020) 108834, https://doi.org/10.1016/j.corsci.2020.108834.

[22] T.L. Burnett, R. Euesden, Y. Aboura, Y. Yao, M.E. Curd, C. Grant, A. Garner, N. J. Henry Holroyd, Z. Barrett, C.E. Engel, P.B. Prangnell, Mechanisms of environmentally induced crack initiation in humid air for new-generation Al-Zn-Mg-Cu alloys, Corrosion 79 (2023) 831–849, https://doi.org/10.5006/4336.

[23] G.M. Scamans, Discontinuous propagation of stress corrosion cracks in Al·Zn·Mg alloys, Scr. Metall. 13 (1979) 245–250, https://doi.org/10.1016/0036-9748(79)90305-3.

[24] S. Lynch, S. Knight, N. Birbilis, B. Muddle, Stress-corrosion cracking of Al–Zn–Mg–Cu alloys effects of composition and heat-treatment, Proc. 2008 Int. Hydrog. Conf. Eff. Hydrog. Mater. (2009) 243–250.

[25] S.P. Knight, K. Pohl, N.J.H. Holroyd, N. Birbilis, P.A. Rometsch, B.C. Muddle, R. Goswami, S.P. Lynch, Some effects of alloy composition on stress corrosion cracking in Al–Zn–Mg–Cu alloys, Corros. Sci. 98 (2015) 50–62, https://doi.org/10.1016/j.corsci.2015.05.016.

[26] R.P. Gangloff, Hydrogen assisted cracking of high strength alloys, Compr. Struct. Integr. 6 (2003).

[27] A.R. Troiano, The role of hydrogen and other interstitials in the mechanical behavior of metals, Metallogr., Microstruct., Anal. 5 (2016) 557–569, https://doi.org/10.1007/s13632-016-0319-4.

[28] H.K. Birnbaum, P. Sofronis, Hydrogen-enhanced localized plasticity—a mechanism for hydrogen-related fracture, Mater. Sci. Eng.: A 176 (1994) 191–202, https://doi.org/10.1016/0921-5093(94)90975-X.

[29] S. Lynch, Hydrogen embrittlement phenomena and mechanisms, Corros. Rev. 30 (2012) 105–123, https://doi.org/10.1515/corrrev-2012-0502.

[30] S.P. Lynch, Environmentally assisted cracking: overview of evidence for an adsorption-induced localised-slip process, Acta Metall. 36 (1988) 2639–2661, https://doi.org/10.1016/0001-6160(88)90113-7.

[31] T. Tsuru, K. Shimizu, M. Yamaguchi, M. Itakura, K. Ebihara, A. Bendo, K. Matsuda, H. Toda, Hydrogen-accelerated spontaneous microcracking in high-strength aluminium alloys, Sci. Rep. 10 (2020) 1998, https://doi.org/10.1038/s41598-020-58834-6.

[32] Y. Xu, H. Toda, K. Shimizu, Y. Wang, B. Gault, W. Li, K. Hirayama, H. Fujihara, X. Jin, A. Takeuchi, M. Uesugi, Suppressed hydrogen embrittlement of high-strength Al alloys by Mn-rich intermetallic compound particles, Acta Mater. 236 (2022) 118110, https://doi.org/10.1016/j.actamat.2022.118110.

[33] K. Shimizu, H. Toda, H. Fujihara, K. Hirayama, K. Uesugi, A. Takeuchi, Hydrogen partitioning behavior and related hydrogen embrittlement in Al-Zn-Mg alloys, Eng. Fract. Mech. 216 (2019) 106503, https://doi.org/10.1016/j.engfracmech.2019.106503.

[34] N.J.H. Holroyd, G.M. Scamans, Stress corrosion cracking in Al-Zn-Mg-Cu aluminum alloys in saline environments, Metall. Mater. Trans. A 44 (2013) 1230–1253, https://doi.org/10.1007/s11661-012-1528-3.

[35] C. Grant, Y. Aboura, T.L. Burnett, P.B. Prangnell, P. Shanthraj, Computational study of the geometrical influence of grain topography on short crack propagation in AA7XXX series alloys, Materialia 29 (2023) 101798, https://doi.org/10.1016/j.mtla.2023.101798.

[36] H. Zhao, P. Chakraborty, D. Ponge, T. Hickel, B. Sun, C.-H. Wu, B. Gault, D. Raabe, Hydrogen trapping and embrittlement in high-strength Al alloys, Nature 602 (2022) 437–441, https://doi.org/10.1038/s41586-021-04343-z.

[37] Y. Wang, B. Sharma, Y. Xu, K. Shimizu, H. Fujihara, K. Hirayama, A. Takeuchi, M. Uesugi, G. Cheng, H. Toda, Switching nanoprecipitates to resist hydrogen embrittlement in high-strength aluminum alloys, Nat. Commun. 13 (2022) 6860, https://doi.org/10.1038/s41467-022-34628-4.

[38] M. Safyari, M. Moshtaghi, S. Kuramoto, On the role of traps in the microstructural control of environmental hydrogen embrittlement of a 7xxx series aluminum alloy, J. Alloy. Compd. 855 (2021) 157300, https://doi.org/10.1016/j.jallcom.2020.157300.

[39] M. Safyari, M. Moshtaghi, T. Hojo, E. Akiyama, Mechanisms of hydrogen embrittlement in high-strength aluminum alloys containing coherent or incoherent dispersoids, Corros. Sci. 194 (2022) 109895, https://doi.org/10.1016/j.corsci.2021.109895.

[40] C.K. Akuata, F.R. Gunawan, P. Suwanpinij, D. Zander, Microstructure evolution and localized corrosion susceptibility of an Al-Zn-Mg-Cu-Zr 7xxx alloy with minor Cr addition, Materials 16 (2023) 946.

[41] A.K. Mukhopadhyay, K.S. Prasad, V. Kumar, G.M. Reddy, S.V. Kamat, V.K. Varma, Key microstructural features responsible for improved stress corrosion cracking resistance and weldability in 7xxx Series Al alloys containing micro / trace alloying additions, Mater. Sci. Forum 519-521 (2006) 315–320, https://doi.org/10.4028/www.scientific.net/MSF.519-521.315.

[42] I.J. Polmear, The influence of small additions of silver on the structure and properties of aged aluminum alloys, JOM 20 (1968) 44–51, https://doi.org/10.1007/BF03378722.

[43] J. Schindelin, I. Arganda-Carreras, E. Frise, V. Kaynig, M. Longair, T. Pietzsch, S. Preibisch, C. Rueden, S. Saalfeld, B. Schmid, J.-Y. Tinevez, D.J. White, V. Hartenstein, K. Eliceiri, P. Tomancak, A. Cardona, Fiji: an open-source platform for biological-image analysis, Nat. Methods 9 (2012) 676–682, https://doi.org/10.1038/nmeth.2019.

[44] C.K. Akuata, L.T. Belkacemi, D. Zander, Revisiting Ag addition in 7xxx aluminum alloys: Insights into its impact on the microstructure and properties of an Al-Zn-Mg-Cu-Zr alloy with a Zn/Mg ratio of 4, Mater. Charact. 215 (2024) 114186, https://doi.org/10.1016/j.matchar.2024.114186.

[45] R. Braun, H.J. Schluter, H. Zuchner, H. Buhl, Hydrogen permeation measurements in aluminium alloy foils, in: A. Turnbull (Ed.), Hydrogen transport and cracking in metals, The Institute of Materials, London, UK, 1995, pp. 280–288.

[46] O. Beyss, D. Zander, Characerization of the effective hydrogen diffusion in overaged 7xxx series Al alloys with a modified Devanathan-Stachurski permeation method, in, ICAA17, Poster-No.299534, 2020.

[47] S. Adhikari, J. Ai, K.R. Hebert, K.M. Ho, C.Z. Wang, Hydrogen in aluminum during alkaline corrosion, Electrochim. Acta 55 (2010) 5326–5331, https://doi.org/10.1016/j.electacta.2010.04.076.

[48] J.-H. Ai, M.L.C. Lim, J.R. Scully, Effective hydrogen diffusion in aluminum alloy 5083-H131 as a function of orientation and degree of sensitization, Corrosion 69 (2013) 1225–1239, https://doi.org/10.5006/0987.

[49] J.-H. Ai, J.R. Scully, Hydrogen diffusivity during corrosion of high-purity aluminum, Corrosion 69 (2013) 752–767, https://doi.org/10.5006/0826.

[50] M.A.V. Devanathan, Z. Stachurski, The adsorption and diffusion of electrolytic hydrogen in palladium, Proc. R. Soc. Lond. Ser. A. Math. Phys. Sci. 270 (1962) 102–190.

[51] ASTM G1 - 03: Standard Practice for Preparing, Cleaning, and Evaluating Corrosion Test Specimens (2017) in, ASTM International, PA USA.

[52] H. Liu, Z. Zhang, D. Zhang, J. Zhang, The effect of Ag on the tensile strength and fracture toughness of novel Al-Mg-Zn alloys, J. Alloy. Compd. 908 (2022) 164640, https://doi.org/10.1016/j.jallcom.2022.164640.

[53] T. Ramgopal, P.I. Gouma, G.S. Frankel, Role of Grain-Boundary Precipitates and Solute-Depleted Zone on the Intergranular Corrosion of Aluminum Alloy 7150, Corrosion, 58 (2002) 687-697 10.5006/1.3287699%J Corrosion.
[54] M. Dumont, W. Lefebvre, B. Doisneau-Cottignies, A. Deschamps, Characterisation of the composition and volume fraction of η′ and η precipitates in an Al–Zn–Mg alloy by a combination of atom probe, small-angle X-ray scattering and transmission electron microscopy, Acta Mater. 53 (2005) 2881–2892, https://doi.org/10.1016/j.actamat.2005.03.004.
[55] L. Ding, L. Zhao, Y. Weng, D. Schryvers, Q. Liu, H. Idrissi, Atomic-scale investigation of the heterogeneous precipitation in the E (Al18Mg3Cr2) dispersoid of 7075 aluminum alloy, J. Alloy. Compd. 851 (2021) 156890, https://doi.org/10.1016/j.jallcom.2020.156890.
[56] M. Conserva, P. Fiorini, Interpretation of quench-sensitivity in Al-Zn-Mg-Cu Alloys, Metall. Trans. 4 (1973) 857–862, https://doi.org/10.1007/BF02643097.
[57] C.K. Akuata, C. Altenbach, C. Schnatterer, P. Suwanpinij, C. Saiyasombat, D. Zander, Age hardening response of AA7108A investigated by means of Synchrotron-based X-ray Absorption Spectroscopy (XAS) measurements, Mater. Sci. Eng.: A 747 (2019) 42–52, https://doi.org/10.1016/j.msea.2019.01.052.
[58] W.F. Smith, N.J. Grant, Effects of chromium and copper additions on precipitation in Al−Zn−Mg alloys, Metall. Trans. 2 (1971) 1333–1340, https://doi.org/10.1007/BF02913356.
[59] Y.-r Zhou, N. Tian, W. Liu, Y. Zeng, G.-d Wang, S.-d Han, G. Zhao, G.-w Qin, Mechanism of heterogeneous distribution of Cr-containing dispersoids in DC casting 7475 aluminum alloy, Trans. Nonferrous Met. Soc. China 32 (2022) 1416–1427, https://doi.org/10.1016/S1003-6326(22)65883-7.
[60] I.J. Polmear, A trace element effect in alloys based on the aluminium-zinc-magnesium system, Nature 186 (1960) 303–304, https://doi.org/10.1038/186303a0.
[61] T. Ogura, S. Hirosawa, A. Cerezo, T. Sato, Atom probe tomography of nanoscale microstructures within precipitate free zones in Al–Zn–Mg(–Ag) alloys, Acta Mater. 58 (2010) 5714–5723, https://doi.org/10.1016/j.actamat.2010.06.046.
[62] Y. Yao, R. Euesden, M.E. Curd, C. Liu, A. Garner, T.L. Burnett, P. Shanthraj, P. B. Prangnell, Effect of cooling rate on the composition and chemical heterogeneity of quench-induced grain boundary η-phase precipitates in 7xxx aluminium alloys, Acta Mater. 262 (2024) 119443, https://doi.org/10.1016/j.actamat.2023.119443.
[63] R. Ayer, J.Y. Koo, J.W. Steeds, B.K. Park, Microanalytical study of the heterogeneous phases in commercial Al-Zn-Mg-Cu alloys, Metall. Trans. A 16 (1985) 1925–1936, https://doi.org/10.1007/BF02662393.
[64] L.F. Mondolfo, Structure of the aluminium: magnesium: zinc alloys, J. Metall. Rev. 16 (1971) 95–124.
[65] Y. Wang, X. Wu, L. Cao, X. Tong, Y. Zou, Q. Zhu, S. Tang, H. Song, M. Guo, Effect of Ag on aging precipitation behavior and mechanical properties of aluminum alloy 7075, Mater. Sci. Eng. A 804 (2021) 140515, https://doi.org/10.1016/j.msea.2020.140515.
[66] S. Hirosawa, Y. Oguri, T. Ogura, T. Sato, Formation mechanisms of precipitate free zones in age-hardenable Al alloys, in: J. Nie, A.J. Morton, B.C. Muddle (Eds.), 9th International Conference on Aluminium Alloys, Institute of Materials Engineering Australasia Ltd, Brisbane, Australia, 2004, pp. 666–671.
[67] J. Peng, S. Bahl, A. Shyam, J.A. Haynes, D. Shin, Solute-vacancy clustering in aluminum, Acta Mater. 196 (2020) 747–758, https://doi.org/10.1016/j.actamat.2020.06.062.
[68] J.K. Park, A.J. Ardell, Precipitation at grain boundaries in the commercial alloy Al 7075, Acta Metall. 34 (1986) 2399–2409, https://doi.org/10.1016/0001-6160(86)90143-4.
[69] G.A. Young, J.R. Scully, Hydrogen production, absorption and transport during environment assisted cracking of an Al-Zn-Mg-(Cu) alloy in humid air, : Int. Conf. Hydrog. Eff. Mater. Behav. Corros. Deform. Interact. (2002) 22–26.
[70] L. Oger, M.C. Lafouresse, G. Odemer, L. Peguet, C. Blanc, Hydrogen diffusion and trapping in a low copper 7xxx aluminium alloy investigated by Scanning Kelvin Probe Force Microscopy, Mater. Sci. Eng.: A 706 (2017) 126–135, https://doi.org/10.1016/j.msea.2017.08.119.
[71] G.M. Pressouyre, A classification of hydrogen traps in steel, Metall. Trans. A 10 (1979) 1571–1573, https://doi.org/10.1007/BF02812023.
[72] J.R. Scully, G.A. Young, Jr, S.W. Smith, Hydrogen solubility, diffusion and trapping in high purity aluminum and selected Al-base alloys, Mater. Sci. Forum 331-337 (2000) 1583–1600, https://doi.org/10.4028/www.scientific.net/MSF.331-337.1583.
[73] J. Chene, I.M. Bernstein, A.W. Thompson, Role of heat treatment and cathodic charging conditions on the hydrogen embrittlement of HP 7075 aluminum alloy, Metall. Trans. A 21 (1990) 455–464, https://doi.org/10.1007/BF02782426.
[74] G.A. Young, J.R. Scully, The diffusion and trapping of hydrogen in high purity aluminum, Acta Mater. 46 (1998) 6337–6349, https://doi.org/10.1016/S1359-6454(98)00333-4.
[75] A. Oudriss, J. Creus, J. Bouhattate, E. Conforto, C. Berziou, C. Savall, X. Feaugas, Grain size and grain-boundary effects on diffusion and trapping of hydrogen in pure nickel, Acta Mater. 60 (2012) 6814–6828, https://doi.org/10.1016/j.actamat.2012.09.004.
[76] M.S. Bhuiyan, H. Toda, Z. Peng, S. Hang, K. Horikawa, K. Uesugi, A. Takeuchi, N. Sakaguchi, Y. Watanabe, Combined microtomography, thermal desorption spectroscopy, X-ray diffraction study of hydrogen trapping behavior in 7XXX aluminum alloys, Mater. Sci. Eng.: A 655 (2016) 221–228, https://doi.org/10.1016/j.msea.2015.12.092.
[77] Y. Iijima, S.-I. Yoshida, H. Saitoh, H. Tanaka, K.-I. Hirano, Hydrogen trapping and repelling in an Al-6 wt% Zn-2 wt% Mg alloy, J. Mater. Sci. 27 (1992) 5735–5738, https://doi.org/10.1007/BF01119730.
[78] T. Tsuru, M. Yamaguchi, K. Ebihara, M. Itakura, Y. Shiihara, K. Matsuda, H. Toda, First-principles study of hydrogen segregation at the MgZn2 precipitate in Al-Mg-Zn alloys, Comput. Mater. Sci. 148 (2018) 301–306, https://doi.org/10.1016/j.commatsci.2018.03.009.
[79] M. Yamaguchi, K.I. Ebihara, M. Itakura, T. Tsuru, K. Matsuda, H. Toda, First-principles calculation of multiple hydrogen segregation along aluminum grain boundaries, Comput. Mater. Sci. 156 (2019) 368–375, https://doi.org/10.1016/j.commatsci.2018.10.015.
[80] L. Oger, B. Malard, G. Odemer, L. Peguet, C. Blanc, Influence of dislocations on hydrogen diffusion and trapping in an Al-Zn-Mg aluminium alloy, Mater. Des. 180 (2019) 107901, https://doi.org/10.1016/j.matdes.2019.107901.
[81] M.S. Bhuiyan, H. Toda, Z. Peng, S. Hang, K. Horikawa, K. Uesugi, A. Takeuchi, N. Sakaguchi, Y. Watanabe, Corrigendum to “Combined microtomography, thermal desorption spectroscopy, X-ray diffraction study of hydrogen trapping behavior in 7XXX aluminum alloys” [Mater. Sci. Eng. A 655 (2016) 221–228, Mater. Sci. Eng.: A 668 (2016) 271–272, https://doi.org/10.1016/j.msea.2016.05.010.
[82] S.P. Knight, N. Birbilis, B.C. Muddle, A.R. Trueman, S.P. Lynch, Correlations between intergranular stress corrosion cracking, grain-boundary microchemistry, and grain-boundary electrochemistry for Al–Zn–Mg–Cu alloys, Corros. Sci. 52 (2010) 4073–4080, https://doi.org/10.1016/j.corsci.2010.08.024.
[83] M. López Freixes, X. Zhou, H. Zhao, H. Godin, L. Peguet, T. Warner, B. Gault, Revisiting stress-corrosion cracking and hydrogen embrittlement in 7xxx-Al alloys at the near-atomic-scale, Nat. Commun. 13 (2022) 4290, https://doi.org/10.1038/s41467-022-31964-3.
[84] W. Gruhl, Stress corrosion cracking of high strength aluminium alloys 75 (1984) 819–826, https://doi.org/10.1515/ijmr-1984-751101.
[85] J.R. Pickens, T.J. Langan, The effect of solution heat-treatment on grain boundary segregation and stress-corrosion cracking of Al-Zn-Mg alloys, Metall. Trans. A 18 (1987) 1735–1744, https://doi.org/10.1007/BF02646205.